processes

MDPI

Article

Numerical Investigation of a Concentration Divider for Ultrasound Calibration Using Constructal Design

Kamille V. Machado [1], Vinicius R. Pepe [2], Fernanda Haeberle [1], António F. Miguel [2,3,*], Flávia S. F. Zinani [1,2,4] and Luiz A. O. Rocha [1,2]

[1] Graduate Program in Mechanical Engineering, Federal University of Rio Grande do Sul, 425 Sarmento Leite St., Porto Alegre 90050-170, RS, Brazil; kamillevieiramachado@hotmail.com (K.V.M.); fernandahaeberle@gmail.com (F.H.); flavia.zinani@ufrgs.br (F.S.F.Z.); luizrocha@mecanica.ufrgs.br (L.A.O.R.)
[2] Complex Flow Systems Lab, Institute of Earth Sciences, Romao Ramalho St. 59, 7000-671 Évora, Portugal; viniciuspepe@gmail.com
[3] School of Science and Technology, University of Évora, Apartado 94, 7002-554 Évora, Portugal
[4] Institute of Hydraulics Research, Federal University of Rio Grande do Sul, 9500 Bento Gonçalves Ave., Porto Alegre 91501-970, RS, Brazil
* Correspondence: afm@uevora.pt

Abstract

This study applies the Constructal Design method to the geometric optimization of a branched symmetric concentration divider for calibrating ultrasound devices used to monitor tumor response with dynamic contrast. Accurate calibration ensures image quality and diagnostic reliability. The geometry consists of a three-dimensional, tree-shaped flow network with two inlets and three outlets, where inlet 1 carries water containing contrast particles, while inlet 2 carries only water. Laminar flow simulations are performed using Computational Fluid Dynamics (CFD) with Ansys Fluent, assuming no-slip wall conditions and zero-pressure outlets. The analysis investigates the effects of the inlet velocity ratio, the diameter ratio, and the vertical positions of the central outlet and inlet tubes, while keeping the total volume and inlet diameter constant. Additionally, velocity, pressure, particle distributions, flow partition ratio, and hydraulic resistance are evaluated. Results show nearly linear concentration responses among the outlets (100%, 50%, and 0%) when the device approaches geometric symmetry with equal inlet velocities, demonstrating efficient control of flow splitting. Although the diameter ratio imposes a trade-off with hydraulic resistance, geometric symmetry combined with Constructal Design promotes improved flow uniformity and enhanced performance, with potential applications in microfluidic mixers that require precise intermediate concentrations.

Keywords: constructal design; geometric symmetry; concentration divider; CFD; ultrasound calibration

Academic Editors: Santiago Laín, Aldo Benavides-Moran, Juan Ricardo Vidal Medina

Received: 27 April 2026
Revised: 1 June 2026
Accepted: 3 June 2026
Published: 5 June 2026

1. Introduction

Dynamic contrast-enhanced ultrasound (DCE-US) was introduced in the 1960s for echocardiographic applications [1]. Initially, this imaging technique relied on the administration of indocyanine dye, a substance frequently used to measure blood flow, which generated a "cloud of echoes" on the echocardiogram, thereby creating a contrast effect in the detected image [2,3]. Due to emerging safety concerns, the clinical use of this initial dye was eventually discontinued, prompting the development of alternative contrast agents.

Significant advances in the technique occurred only in the 1990s with the introduction of intravenously administered microbubble contrast agents mainly composed of the inert gas sulfur hexafluoride (SF_6) [4]. After injection, these microbubbles increase the acoustic impedance difference between blood and surrounding tissues, enabling real-time, high-contrast visualization of vascular structures and organ perfusion [5].

Due to its high diagnostic accuracy, particularly for the early detection of vascular and antiangiogenic pathologies, the clinical application of DCE-US has significantly increased over the last few decades. Studies have highlighted that the diagnostic reliability of the technique strongly depends on the stability of the acoustic response produced by the contrast-agent microbubbles [6–9]. In this context, periodic calibration of DCE-US systems is essential, as ultrasound signal intensity is directly related to microbubble concentration, a parameter that strongly influences image quality and reproducibility. Currently, calibration of DCE-US systems is predominantly performed through experimental procedures that manually prepare different contrast-agent concentrations. However, this approach tends to introduce operational variability, high contrast-agent consumption, increased experimental cost, and long execution times, while limiting the acquisition of local flow parameters. Studies such as those by [10–15] emphasized the need for more standardized, reproducible calibration methodologies for quantitative ultrasound imaging systems.

In this scenario, the application of Computational Fluid Dynamics (CFD) combined with concentration-divider devices emerges as a promising alternative for passively generating predictable and controlled intermediate microbubble concentrations. Besides reducing experimental waste, such systems may improve calibration repeatability and support quality-control procedures for clinical imaging protocols.

In a recent study, a device was developed to analyze variations in particle concentration using a system designed around a concentration divider with two inlets and five outlets [16]. That study aimed to simulate flow under conditions of simultaneous variation in contrast agent concentrations, while preserving the classical laws of fluid flow. The authors observed that the ideal concentration gradient, namely, the one that best represents the imaging response, occurs when the particle concentrations at the outlets are linear (e.g., 100%, 75%, 50%, 25%, and 0% for outlets 1, 2, 3, 4, and 5, respectively) [17,18]. An analysis of the study by [16] reveals clear opportunities for further flow analysis in engineering applications, where improving system performance by reducing pressure losses and increasing efficiency is paramount. System performance can be further enhanced through several strategies, such as material variation, structural modifications, and geometric optimization.

Here, the Constructal Law, introduced by Adrian Bejan, explains how shapes and designs develop in nature [19–21]. The law says: "For a finite-size flow system (not infinitesimal) to persist in time (to live), it must evolve freely in such a way that it provides easier and greater access to the currents that flow through it." In engineering, Constructal Design means intentionally designing flow systems within certain space limits. This method has been used in many areas and often leads to very effective and efficient results. In contrast to traditional computational fluid dynamics (CFD) parameter optimization, which typically utilizes algorithmic or black-box methods to independently adjust dimensions in pursuit of a mathematical minimum, Constructal Design is grounded in physical principles [21]. This methodology assesses the evolution of flow architecture under global constraints, such as fixed total system and tube volumes. By systematically exploring geometric degrees of freedom while upholding these finite-size constraints [19–21], Constructal Design explicitly elucidates the physical trade-offs that govern the system. As a result, it not only determines the optimal configuration but also offers a fundamental physical rationale for why a particular architecture most effectively facilitates flow.

To further optimization within a medical context, this paper presents a Computational Fluid Dynamics (CFD) approach to investigate a calibration device for DCE-US systems within the Constructal Design framework. This is applied by granting the system the freedom to adapt while systematically varying the geometry and flow velocity across different Reynolds numbers, keeping the inlet tube diameter and the total volume constant. Specifically, the constructal method is applied to the geometry shown in Figure 1, which is based on a concentration divider with two inlets and three outlets, corresponding to stage 1 of the geometry presented in the reference study [16,22,23]. The numerical simulations evaluate three degrees of freedom: variation in the geometric diameter of the outlet tubes, variation in the vertical position of outlet tube 2, and variation in the inlet flow velocity 1.

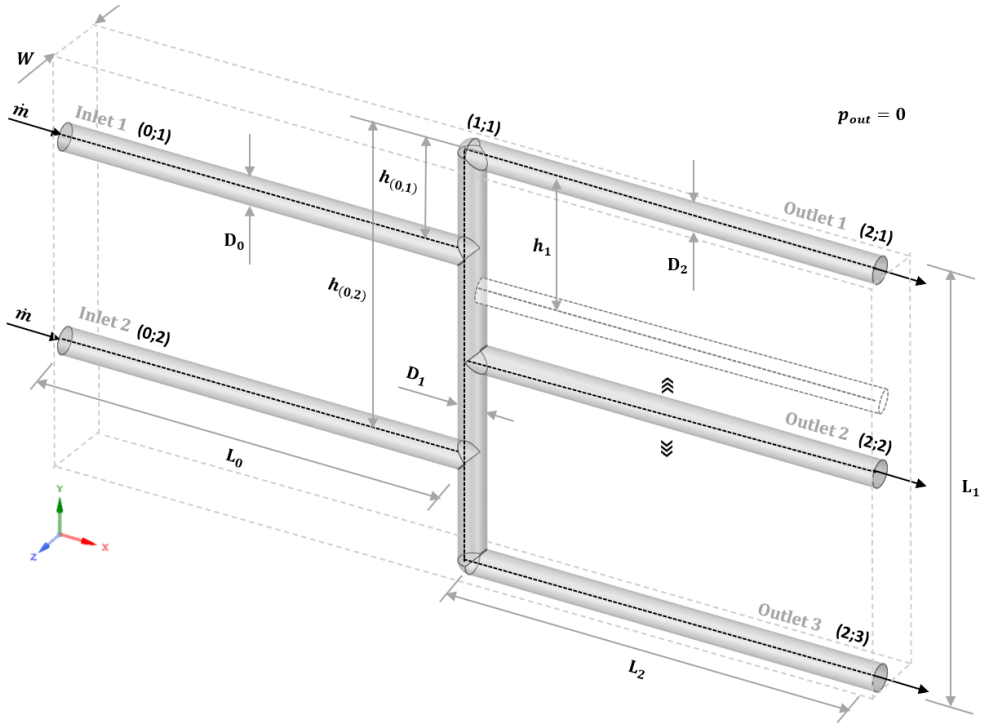

Figure 1. Geometric arrangement of DCE-US based on a concentration divider.

This study examines the influence of device asymmetry on the calibration of ultrasound equipment. Geometric asymmetry arises when the position, length, and diameters of the daughter tubes, which originate from the main branch, differ from those of the parent tube. Although prior research on tree-shaped networks has addressed asymmetries in device length and diameter, the present study further investigates asymmetry associated with the vertical position of outlet tube 2.

Understanding asymmetric branching is critical because it affects flow resistance both locally and throughout the entire network, making the analysis of its impact on the system's response essential [24]. Previous studies examined the hydrodynamic performance of T- and Y-shaped branching structures with symmetric and asymmetric binary configurations. These studies demonstrated that the degree of asymmetry at each bifurcation affects the overall performance of the tree network, showing that symmetric geometries do not always yield the best performance [24,25]. Consequently, the primary aim of this study is to determine the most efficient and cost-effective geometries, operating conditions, and calibration procedures for a DCE-US concentration divider. Specifically, this work aims to address the following critical research questions: (i) How can Constructal Design principles be applied to geometrically optimize the flow architecture of a concentration divider to achieve a linear particle concentration gradient across its outlets? and

(ii) What geometric parameters are most critical to the design and performance of this device for medical ultrasound calibration?

2. Materials and Methods

2.1. Problem Description

The present study addresses the application of the Constructal Design method to the calibration of dynamic contrast-enhanced ultrasound devices, in which we performed computational numerical simulations in ANSYS Fluent 2025/R1 based on the concentration divider illustrated in Figure 1. The device consists of a three-dimensional configuration with two inlets and three outlets.

The geometric arrangement has a constant diameter at both inlets and a constant total occupied volume ($\forall = 6.00 \times 10^3$ mm^3). In addition, this study assumes the volume ratio (φ) to be a global constant, defined as the ratio of the volume occupied by the tubes to the total system volume. The tubes occupy 10% of the total volume ($\forall_T = 600$ mm^3), resulting in $\varphi = 0.10$.

The study is conducted based on particle concentration analysis, focusing on variations in the concentration of contrast-agent particles. Inlet 1 contains both the continuous and discrete phases (water and particles), whereas inlet 2 contains only the continuous phase. The study aims to determine the particle concentration at each outlet and to identify the set of degrees of freedom that define a more efficient device, that is, the geometric configuration and flow velocity that produce a linear response with particle concentrations of 100%, 50%, and 0% at outlets 1, 2, and 3, respectively.

To this end, the Constructal Design method is applied by implementing degrees of freedom subject to two constraints (global constants): a constant inlet tube diameter and constant volumes. The degrees of freedom are applied with respect to variations in the outlet diameter (D_2), the vertical position of outlet tube 2, and the variation in the inlet flow velocity at inlet 1.

Regarding vertical variation, represented by the ratio of the distance between outlets (α), the symmetric configuration occurs when $\alpha = 0.500$, corresponding to equally spaced outlet tubes. Asymmetric configurations ($\alpha \neq 0.500$) allow evaluating the effect of unequal tube positions on the device's performance. The comparative analysis of symmetric and asymmetric scenarios highlights how geometric asymmetry influences calibration and device optimization, emphasizing its fundamental role in Constructal Design.

$$\forall = (L_0 + L_2)WL_1, \tag{1}$$

$$\forall_T = \frac{2\pi L_0 {D_0}^2}{4} + \frac{\pi L_1 {D_1}^2}{4} + \frac{3\pi L_2 {D_2}^2}{4}, \tag{2}$$

$$\varphi = \frac{\forall_T}{\forall}, \tag{3}$$

where $\forall$ denotes the total volume occupied by the arrangement, $\forall_T$ corresponds to the tube volume, W is the depth of the bounding domain equal 2.96 mm for all cases, D_0 and L_0 represent the diameter and length of the inlet tubes, D_1 and L_1 denote the diameter and length of the vertical tube, and D_2 and L_2 correspond to the diameter and length of the outlet tubes. The bounding depth W naturally differs from the inner tube diameter because it defines the outer physical limit of the 3D fluid-dynamic region modeled in our CFD domain, securely accommodating the spatial arrangement of the entire branched network.

To execute the optimization, the system is parameterized using three geometric degrees of freedom and one operational parameter. The geometric degrees of freedom dictate the flow architecture and are defined as follows:

$$aD = \frac{D_2}{D_1}, \tag{4}$$

$$\alpha = \frac{h_1}{L_1}, \tag{5}$$

where aD represents the ratio between the diameter of the vertical tube (D_1) and the outlet diameter (D_2). Because the total volume of the tubes is constrained as a global constant (a fundamental requirement of Constructal Design to ensure optimization occurs under finite-size material constraints), any variation in the diameter ratio aD necessitates a proportional adjustment in the tube lengths to maintain volume closure. The parameter α represents the ratio of the distance between outlet tubes 1 and 2 (h_1) to the total length of the vertical tube (L_1). Consequently, a symmetric placement corresponds to the precise midpoint of the vertical tube, yielding α = 0.500, whereas α = 1.00 would indicate an asymmetric position at the extreme distal end of the structure.

Additionally, a degree of freedom was introduced to evaluate particle concentration as a function of the vertical variation in the inlet tubes, represented by the dimensionless parameter (δ). This parameter defines the relative vertical location of the inlet tubes with respect to the central axis of the system. Specifically, δ determines the exact vertical distances $h_{(0,1)}$ (representing the position of Inlet 1) and $h_{(0,2)}$ (representing the position of Inlet 2) relative to the total vertical length L_1. Accordingly, it became necessary to define the vertical position of inlet tube 1 using two distinct sets of equations.

The first set corresponds to cases in which the distance between the inlet tubes remains constant, while both tubes are vertically displaced together, either upward (δ = 0.250) or downward (δ = 0.750). The second set represents configurations in which the inlet tubes positions vary relative to the central axis of the system. In these cases, the tubes may be positioned closer together (δ = 0.150) or farther apart (δ = 0.850).

$$h_{(0,1)} = \begin{cases} \left(\frac{L_1}{2}\right)\delta & \delta = 0.250, 0.750 \\ \left(\frac{L_1}{2}\right)(1-\delta) & \delta = 0.150, 0.850 \end{cases}, \tag{6}$$

where δ represents the dimensionless parameter associated with the vertical variation in the inlet tubes, $h_{(0,1)}$ denotes the vertical position of inlet tube 1 relative to the upper end of the vertical tube, and L_1 is the length of the vertical tube.

Finally, alongside the geometric variations, an operational parameter was introduced to assess the effect of boundary flow asymmetry. This is defined by the inlet velocity ratio

$$\psi = \frac{u_{in\,(0;1)}}{u_{in\,(0;2)}}, \tag{7}$$

where ψ represents the ratio of the velocity in inlet tube 1 ($u_{in(0;1)}$) to the velocity in inlet tube 2 ($u_{in(0;2)}$).

Table 1 presents the dimensional data of the symmetric geometry (D_0 = 2.00 mm, α = 0.500, φ = 0.10 and W = 2.96 mm) used to represent the concentration divider employed to calibrate a dynamic contrast-enhanced ultrasound device, as shown in Figure 1.

Thus, this study geometrically parameterizes the concentration divider used to calibrate the DCE-US device in ANSYS 2025/R1 DesignModeler. The study evaluates the following parameters: three outlet diameter ratios (aD), considering equal diameters, 20% smaller, and 40% smaller outlet diameters (1.00, 0.80, and 0.60); five vertical positions of outlet tube 2 (0.150, 0.325, 0.500, 0.675, and 0.850); and four inlet flow velocity ratios (1.20, 1.00, 0.80, and 0.60). For each adopted velocity ratio, a corresponding Reynolds number of 420, 350, 280 and 210 was considered.

Table 1. Dimensions of the arrangement based on a symmetric geometry.

Parameter	Length (mm)
L_0	31.83
L_1	31.83
L_2	31.83
D_0	2.00
D_1	2.00
D_2	2.00

Regarding the vertical position of outlet tube 2, the two extreme values analyzed (0.150 and 0.850) correspond to the positions immediately above inlet 1 and below inlet 2, respectively. Likewise, the symmetric position corresponds to $\alpha = 0.500$.

Figure 2 illustrates the degrees of freedom and constants used in the ultrasound calibration study. Based on this combination of degrees of freedom, the present study comprises 240 configurations, 60 of which involve geometric variations (outlet diameter, the position of outlet tube 2, and the position of inlet tubes), combined with 4 inlet flow velocities at inlet 1.

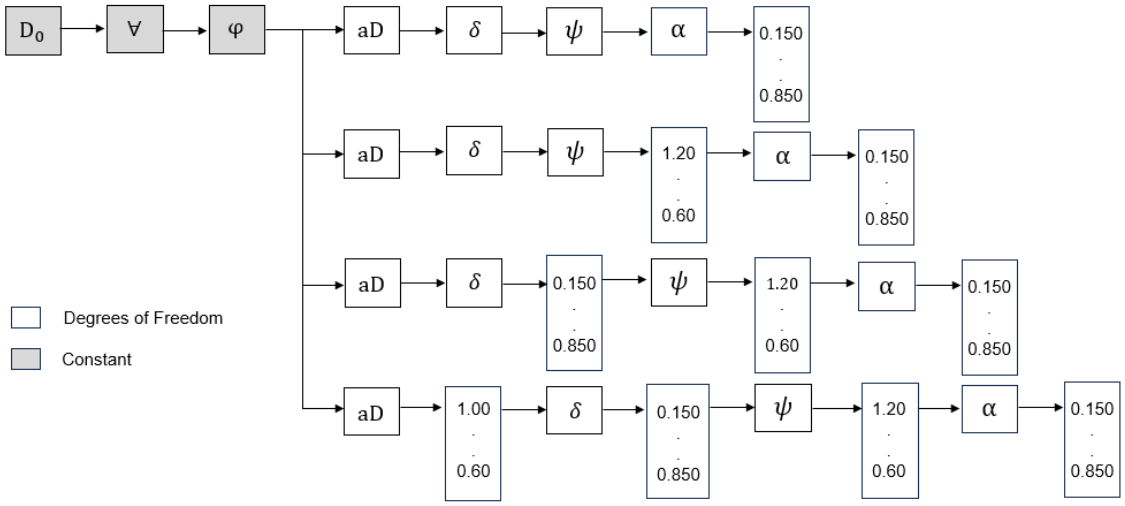

Figure 2. Scheme of constants and degrees of freedom applied in the study.

For the present study, we performed particle analysis using a Lagrangian approach, in which the model solves the equations of motion for each particle at all time steps within the flow field.

The study considers laminar flow and the following boundary conditions: a prescribed inlet velocity, no-slip conditions at the walls, and zero-gauge pressure at the outlets. The governing equations for the conservation of mass and momentum of the fluid (water) are the incompressible Navier–Stokes equations and the continuity equation, expressed in Equations (8) and (9), respectively [26].

$$\nabla \cdot \mathbf{u} = 0, \tag{8}$$

$$\rho \frac{\partial \mathbf{u}}{\partial t} + \rho(\mathbf{u} \cdot \nabla)\mathbf{u} = -\nabla p + \mu \nabla^2 \mathbf{u}, \tag{9}$$

where $\mathbf{u}$ is the velocity vector, ρ is the fluid density, μ is the dynamic viscosity, and p is the pressure.

In addition, the variation in flow velocity was performed through changes in the Reynolds number based on the inlet tube diameter:

$$\mathrm{Re} = \frac{u\rho D_0}{\mu}, \quad (10)$$

To conduct the particle-based study, we used the Discrete Phase Model (DPM) in ANSYS Fluent 2025/R1. The DPM accounts for the interaction between the continuous and discrete phases, which in this study are represented by water and the SonoVue contrast agent [27]. The study performs the computational numerical simulations under transient conditions, with a total simulation time of 90 s. During this period, the system continuously injected 10^6 particles into the flow at each time step. In addition, both the water and the particles were assumed to remain at ambient temperature (T_{amb}) of 20.00 °C. This baseline temperature is heavily representative of standardized benchtop calibration environments for ultrasound devices. While minor ambient temperature fluctuations (e.g., ±1 °C) will slightly alter fluid viscosity, the resulting variations in the laminar Reynolds number are mathematically negligible and do not fundamentally shift the topological flow partitioning or particle distribution trends discussed herein.

In this context, the study adopts a Lagrangian approach to track the motion of individual spherical particles within the flow. The force balance acting on each particle, which the model integrates to determine its trajectory, is given by the Basset–Boussinesq–Oseen formulation [28]:

$$\frac{d\mathbf{u}_p}{dt} = \frac{1}{\rho_p}\left[\frac{18\mu}{D_p^2}\frac{C_D\,\mathrm{Re}_p}{24}\left(\mathbf{u}-\mathbf{u}_p\right) + \frac{1}{2}\rho\frac{d}{dt}\left(\mathbf{u}-\mathbf{u}_p\right) + \mu\mathbf{u}_p\frac{du}{dt} + g\left(\rho_p-\rho\right) + F_{br}\right], \quad (11)$$

where $\mathbf{u}$ is the fluid velocity and $\mathbf{u}_p$ is the particle velocity; g is the gravitational acceleration; ρ_p is the particle density; C_D is the drag coefficient; D_P is the particle diameter; and Re_p is the particle Reynolds number. The five terms on the right-hand side of the equation represent, respectively: the drag force (first term), the virtual mass force required to accelerate the fluid surrounding the particle (second term), the force due to the fluid pressure gradient (third term), the gravitational force (fourth term), and the force resulting from Brownian collisions (fifth term).

In this configuration, inlet 1 contains both the continuous phase (water) and the discrete phase (particles), whereas inlet 2 contains only the continuous phase. The study evaluates particle tracking using the Discrete Phase Model (DPM) based on the number of particles exiting through outlet 1. Thus, the percentage of particles leaving through each outlet ($\beta_{(2,i)}$) is defined relative to the number of particles passing through outlet 1, as expressed by:

$$\beta_{(2,i)} = \frac{\beta_{out(2,i)}}{\beta_{out(2,1)}} \cdot 100\%, \quad (12)$$

where $\beta_{out(2,i)}$ and $\beta_{out(2,1)}$ correspond to the particle concentration exiting through outlet i (where i denotes the outlet number) and through outlet 1, respectively.

In addition, for a 90 s simulation, considering the properties of the contrast agent and the diameter of each spherical particle, it is possible to determine the mass flow rate of each flowing particle, as defined by:

$$\dot{m}_p = N_p \rho_p \forall_p, \quad (13)$$

where $\dot{m}_p$ is the particle mass flow rate, N_p corresponds to the number of particles per unit time in the flow, ρ_p is the particle density, and $\forall_p$ corresponds to the particle volume.

Table 2 summarizes the system parameters adopted in the numerical simulations of the three-dimensional concentration divider. The study assumes laminar flow and imposes a convergence criterion of at least 1×10^{-4} for both the velocity and continuity equations to ensure numerical accuracy. The simulations are run at ambient temperature with stationary isothermal walls. Therefore, the model does not solve the energy equation. The numerical model discretizes and solves the governing equations using the coupled pressure–velocity scheme, thereby enhancing solution stability for the investigated flow conditions. The model

prescribes zero-pressure boundary conditions at the outlets, allowing an appropriate evaluation of the concentration distribution and flow behavior within the divider.

Table 2. Boundary conditions for the particle concentration study.

Water	Value (Unit)	Particle	Value (Unit)
$T_{0,1}$	20.00 (°C)	T_{part}	20.00 (°C)
$T_{0,2}$	20.00 (°C)	N_p	10^6 (1/s)
P_{out}	0.00 (Pa)	D_p	3.00 (µm)
µ	1.0016×10^{-3} (Pa s)	$\forall_p$	1.414×10^{-17} (m^3)
ρ	998.20 (kg/m^3)	ρ_p	3.16×10^{-3} (kg/m^3)

To quantify flow asymmetry, this study defines the dimensionless Flow Partition Ratio (FPR) as the ratio of the mass flow rate through a specific tube to the total mass flow rate through the tree-shaped flow network [26,29]. This dimensionless parameter quantifies the extent to which the flow entering the device is evenly distributed among the network's outlets. In the present case, for example, the optimal configuration corresponds to an FPR of 0.33 for outlets 1, 2, and 3, representing a proportional distribution of the 100% mass flow rate entering the device. Accordingly, FPR is defined as:

$$FPR_{(2,i)} = \frac{\dot{m}_{(2,i)}}{\dot{m}}, \quad (14)$$

where $\dot{m}_{(2,i)}$ is the outlet mass flow rate of the tubes, where i represents each of the outlets 1, 2, and 3, and $\dot{m}$ is the inlet total mass flow rate of the device.

Another factor analyzed in this study is the flow resistance:

$$R = \frac{\Delta p}{\dot{m}}, \quad (15)$$

where R is the flow resistance, Δp is the pressure difference (Pa), and $\dot{m}$ is the total mass flow rate at the two inlets. This analysis assesses how flow behavior changes as a function of the degrees of freedom applied.

2.2. Objectives and Objective Function

The main objective of this study is to develop an analysis based on the concepts of Constructal Theory to achieve a more efficient and cost-effective calibration of equipment. Accordingly, the analysis consists of:

- Developing a computational numerical study applying the Constructal Design method to concentration dividers used for ultrasound calibration.
- Identifying which combination of variables associated with the degrees of freedom proposed in the Methodology section provides the best linear response, namely particle concentrations of 100%, 50%, and 0% at outlets 1, 2, and 3, respectively.

The application of Constructal Theory in this study aims to develop new geometric structures and to promote interdisciplinary integration by combining engineering concepts with medical applications, thereby enriching the scientific literature.

The objective function (OF) of the study is formulated to quantify deviations from the ideal linear response across the device's outlets, enabling us to identify the optimal combination of degrees of freedom.

$$OF = \min_{aD;\ \alpha;\ \psi} \left(S_P = \sum_{i=1}^{3} \left| \beta_{(2,i)} - \beta_{(ref,i)} \right| \right) \quad (16)$$

where S_P represents the total absolute error, $\beta_{(2,i)}$ is the simulated particle concentration at outlet i, and $\beta_{(ref,i)}$ is the ideal target concentration for outlet i (specifically 100%, 50%, and 0% for i = 1, 2, and 3, respectively).

This formulation represents a minimization problem that aims to drive the total absolute error, Sp, as closely as possible to zero. Achieving a value of zero would indicate that the chosen combination of geometric and flow parameters perfectly reproduces the ideal, linear calibration targets across all three outlets.

2.3. Mesh Study and Time-Step Independence Study

We conducted the mesh study using the Grid Convergence Index (GCI) [30,31] and analyzed results for different mesh sizes. For the present study, we performed a convergence analysis of the particle concentration escaping through outlet 2. Smaller diameters produce the critical values. In this sense, we verified that among the possible geometric variations, the smallest diameters appear when the diameter ratio (aD) equals 0.60.

For the GCI test, we used three different element sizes in a hexahedral mesh, including 10 inflation layers near the wall with an initial thickness of 0.05 mm. These layers become progressively finer close to the surface to accurately capture velocity gradients and other flow properties in the near-wall region. The refined mesh has an element size of 0.0823 mm, while the intermediate and coarse meshes have element sizes of 0.1089 mm and 0.1425 mm, respectively.

Table 3 presents the results of the mesh independence study based on the particle concentration at outlet 2 $\beta_{(2,2)}$ and the flow resistance (R). It is observed that $\beta_{(2,2)}$ exhibits a more pronounced variation between the coarse and medium meshes (from 40.37% to 44.86%), indicating sensitivity to spatial discretization within this range. However, the difference between the medium and fine meshes is below 2%, suggesting a trend toward solution convergence.

For the flow resistance (R), variations across the meshes are below 4%, indicating monotonic behavior and lower sensitivity to mesh refinement. The calculated Grid Convergence Index (GCI) values indicate low numerical uncertainty for both variables in the finer meshes, although the discrepancy observed between the coarse and medium meshes for $\beta_{(2,2)}$ suggests caution when interpreting the GCI in isolation.

Considering the trade-off between computational cost and accuracy, the coarse mesh was selected for all subsequent simulations. While there is a localized sensitivity in $\beta_{(2,2)}$ between the coarse and medium meshes, the global flow resistance (R) remains highly stable. Thus, the coarse mesh proved sufficient to accurately capture the qualitative trends and comparative performance of the geometries without incurring excessive computational expense. To contextualize this trade-off, the full parametric study required 240 distinct three-dimensional, transient simulations with discrete phase tracking over 90 s of flow time. Employing a medium or fine mesh across the entire matrix would have been computationally impractical due to the high computational cost and execution time. Because the coarse mesh successfully captured the stable, global hydrodynamic behaviors and qualitative concentration trends, it was deployed as a comparative screening tool to efficiently navigate the broad design space. The localized absolute sensitivities in particle concentration were subsequently mitigated by subjecting only the final optimized configurations to the high-resolution validation detailed in Section 3.2. Subsequently, a time-step sensitivity analysis was conducted on the selected coarse mesh. The relative error was evaluated, as shown in Table 4.

The results indicate that the difference between the time-steps of 0.10 s and 0.05 s is 1.18%, suggesting weak sensitivity within this range. Although further refinement to a time-step of 0.01 s yielded a higher relative difference of 7.41% for $\beta_{(2,2)}$, the global flow resistance remained entirely insensitive to temporal discretization. Given the exponentially higher computational cost associated with smaller time steps, 0.05 s was established as the optimal compromise to provide reliable, comparable transient data. This choice corresponds to 1800 time-steps for a total simulation time of 90 s.

The relative errors for the particle concentration and flow resistance are calculated using the following formulations

$$\varepsilon_{(2,2)} = \left|\frac{\beta_{(i)} - \beta_{(i-1)}}{\beta_{(i)}}\right| 100\%, \quad (17)$$

$$\varepsilon_{(R)} = \left|\frac{R_{(i)} - R_{(i-1)}}{R_{(i)}}\right| 100\% \quad (18)$$

Mesh convergence tests are inherently broad; however, literature establishes that for GCI values of 5% or lower, further mesh refinement results in negligible changes to the flow field [29,32,33]. Additional refinement would unnecessarily inflate computational costs. Consequently, this 5% threshold was adopted as the reference limit for both the GCI and the relative error analyses in this study. Figure 3 illustrates the hexahedral mesh with a coarse element size of 0.1425 mm, which we selected for all simulations.

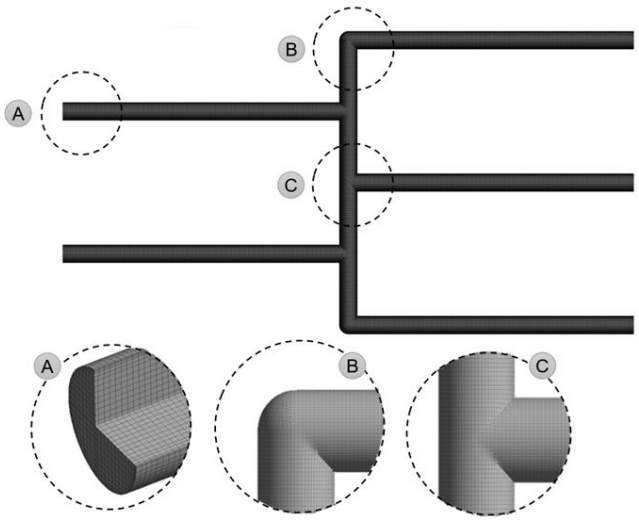

Figure 3. Representation of the coarse mesh of a symmetric arrangement based on a concentration divider, determined by the GCI method, where the details show: (**A**) the inlet region with inflation layers; (**B**) the corner region; and (**C**) the junction region.

Table 3. Mesh convergence test (GCI) for the particle concentration study.

aD	D_2 (mm)	Mesh Type	Mesh Element	Element Size (mm)	$\beta_{(2,2)}$ (%)	GCI (%)	R (Pa s/kg)	GCI (%)
0.60	1.20	Course	458,914	0.1425	40.37	1.62	521,329.25	4.42
		Medium	916,195	0.1089	44.86	0.17	525,605.77	3.56
		Fine	2,624,843	0.0823	44.35	-	529,240.52	-

Table 4. Time independence test for the particle concentration study.

aD	D_2 (mm)	Element Size (mm)	Time-Step (s)	$\beta_{(2,2)}$ (%)	$\varepsilon_{(2,2)}$ (%)	R (Pa. s/kg)	$\varepsilon_{(R)}$ (%)
0.60	1.20	0.1425	0.10	40.37	-	521,329.25	-
		0.1425	0.05	40.84	1.18	521,329.69	0.00
		0.1425	0.01	37.82	7.41	521,330.12	0.00

2.4. Model Validation

To establish a baseline for performance, this study defines an ideal calibration as one exhibiting a perfectly linear trend, corresponding to particle concentrations of 100%, 50%, and 0% at outlets 1, 2, and 3, respectively. The numerical model validated herein utilizes a symmetric geometry with an inlet diameter of D_0 = 2.00 mm. As shown in Figure 4, the simulated results exhibit a linear trend with decreasing particle concentrations across the

analyzed outlets, closely mirroring the ideal target. In comparison with the reference study by [16], the present study (D_0 = 2.00 mm) yields a particle concentration at outlet 2 of 56.23%, representing a relative difference of approximately 4.21%. This is considered acceptable within the established limit of up to 10% deviation for numerical validation. When analyzing our previous study (D_0 = 3.00 mm) [33], numerical differences are expected and observed, which are physically attributed to variations in the geometric diameter and, consequently, the flow velocity and Reynolds number.

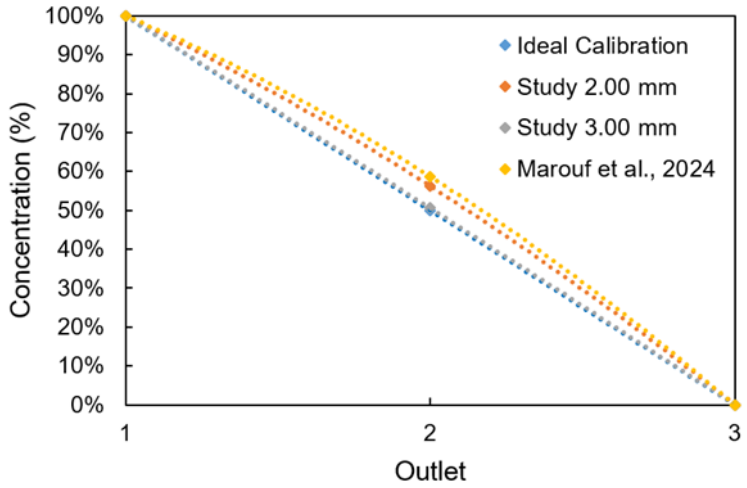

Figure 4. Comparison of simulated particle concentrations across outlets against literature and ideal targets [16].

Table 5 presents the numerical values obtained in the present study, along with the reference values used for validation. These validation cases assume a symmetric geometry with uniform inlet flow conditions. Relative errors were calculated to quantify the accuracy of the present model against both the ideal targets and the literature data.

Table 5. Numerical data of the particle concentration validation study.

Nº	Studies	Outlet 1	Outlet 2	Outlet 3	$\varepsilon_{(2\text{-}1)}$	$\varepsilon_{(2\text{-}3)}$	$\varepsilon_{(2\text{-}4)}$
1	Ideal Calibration	100.00%	50.00%	0.00%	12.46%	-	-
2	Present study (D_0 = 2.00 mm)	100.00%	56.23%	0.00%	-	-	-
3	Previous study [15] (D_0 = 3.00 mm)	100.00%	50.57%	0.00%	-	11.18%	-
4	Marouf et al., 2024 [16]	100.00%	58.70%	0.00%	-	-	4.21%

3. Results

This section presents the results obtained by applying three degrees of freedom: variation in the diameter ratio (aD), variation in the vertical position of outlet tube 2 (α), and the ratio between the inlet velocities (ψ). To evaluate the influence of scale, the results for the current geometry (D_0 = 2.00 mm) are directly compared with those from a previous study with D_0 = 3.00 mm.

3.1. Comparative Study of Geometries with Different Inlet Diameters

Figure 5 illustrates the behavior of the particle concentration response at outlet 2 as a function of the variation in the vertical position of the tube (α) and the ratio between the inlet velocities (ψ). The graph on the left shows the variation in particle concentration at outlet 2 as a function of the central tube position for cases with D_0 = 2.00 mm and D_0 = 3.00 mm. In this analysis, both the diameter ratio (aD = 1.00) and the inlet velocity ratio (ψ = 1.00) were kept constant. In turn, the graph on the right represents the variation in particle

concentration at outlet 2 as a function of the inlet velocity ratio (ψ), for the same values of D_0. In this case, the diameter ratio (aD = 1.00) and the central tube position, assumed to be symmetric (α = 0.500), were kept constant.

Figure 5 indicates that, when only the vertical position of outlet tube 2 is considered, the curves exhibit strong similarity despite changes in inlet diameter. The trends follow a third-order polynomial, with optimal calibration (50% fraction at outlet 2) occurring between positions 0.300 and 0.500, close to inlet tube 1 and the plane of symmetry.

For a symmetric geometry, variations in the inlet velocity ratio produce more results that are scattered as the inlet diameter of the device changes, which is expected since diameter variations directly affect the Reynolds number and the flow velocity. Nevertheless, we observe intersection points between the two trend curves. For velocity ratios near 0.90 and 1.00, both curves yield particle concentrations at outlet 2 that are close to the ideal calibration value of 50%.

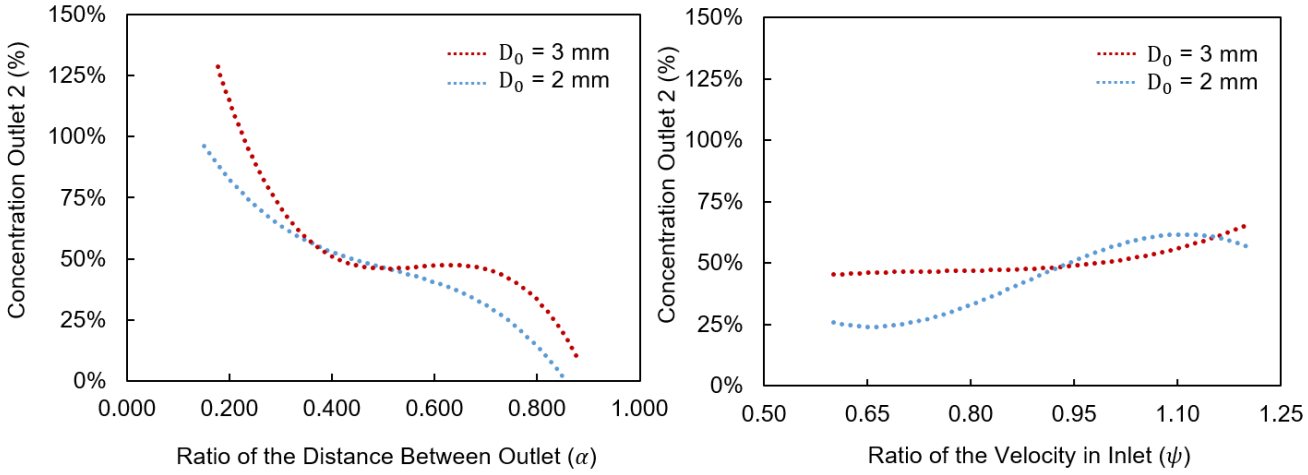

Figure 5. Comparative study of particle concentration at outlet 2. The (**left**) graph illustrates concentration as a function of the vertical position (α) at a constant velocity ratio, while the (**right**) graph shows concentration as a function of the inlet velocity ratio (ψ) at a symmetric position. Both graphs compare inlet diameters of 2.00 mm and 3.00 mm.

Based on these graphs, the analysis shows that variations in the vertical position of outlet tube 2 produce similar trend curves despite changes in the inlet diameters. The results also indicate that the best calibration response occurs near the symmetry condition. The same behavior, where outlet 2 more frequently reached values near 50%, is observed in [33]. However, variations in diameter alter the flow velocity, which explains the behavior observed in the results as a function of the inlet velocity ratio. Furthermore, the results show that conditions closer to symmetry and with equal inlet velocities tend to yield values approaching the ideal calibration condition.

To further analyze the response behavior at outlet 2, a study was conducted that considered the two degrees of freedom acting simultaneously: variations in vertical position and in the inlet velocity ratio.

Figure 6 shows the trend lines for each inlet velocity ratio as a function of the vertical position of outlet tube 2, for studies conducted with inlet diameters of 2.00 mm and 3.00 mm. However, for the 2.00 mm diameter, lower velocity ratios ψ reflect a reduction in the particle concentration percentage at α = 0.150. For the case of a 2.00 mm diameter, a point close to the ideal calibration value of 50% is observed when α is approximately 0.400, with velocity ratios ψ equal to 1.20 and 1.00, that is, when the inlet velocity at inlet 1 is 20% higher than that at inlet 2 or when both inlet velocities are equal. For the configuration with an outlet diameter D_0 = 3.00 mm, the trend curves show two intersection points,

indicating a transition in the dominant mechanism that controls the concentration distribution at outlet 2. The first intersection occurs at $\alpha \approx 0.400$ between the velocity ratios $\psi = 0.60$ and $\psi = 1.00$, while the second occurs at $\alpha \approx 0.600$ between $\psi = 0.80$ and $\psi = 1.00$. These intersections indicate that the influence of the inlet velocity ratio and the geometric configuration become comparable at specific values of α. As α increases, the geometric asymmetry imposed by the vertical displacement of outlet tube 2 progressively alters the hydraulic pathways and modifies the flow partition within the device. Studies of flow distribution in T-shaped junctions and tree-shaped flow networks report similar behaviors, where the interaction between boundary conditions and geometric configuration determines the final flow partition [20,24].

Accordingly, the results depicted in Figure 6 show that both analyzed diameters exhibit similar calibration points at α values close to 0.400, with equal inlet flow velocities (i.e., $\psi = 1.00$).

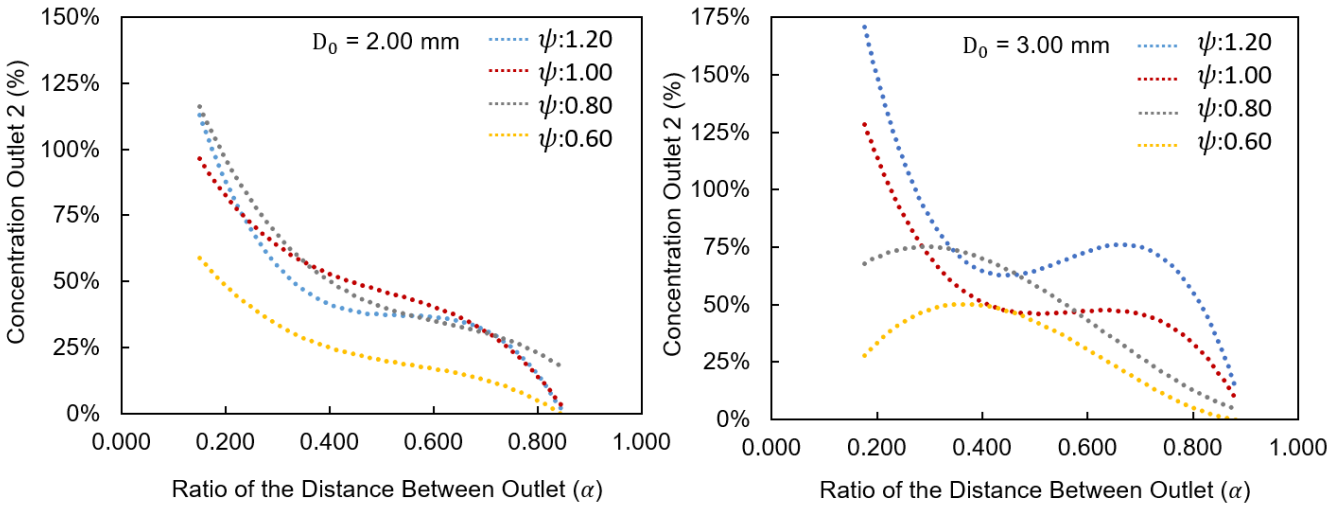

Figure 6. Particle concentration at outlet 2 as a function of the vertical position (α) across multiple inlet velocity ratios (ψ). The analysis compares geometries with 2.00 mm (**left**) and 3.00 mm (**right**).

3.2. Particle Concentration Analysis Based on the Application of Degrees of Freedom

At this stage of the study, the analysis focused on a geometry with an inlet diameter of $D_0 = 2$ mm, as this diameter matches that investigated in the reference study [16].

Regarding the application of the degrees of freedom, Figure 7 shows the particle concentration for the different geometric variations performed for each inlet velocity ratio. In this context, the results indicate that across all four analyzed values of the inlet velocity ratio ψ, the particle concentration at outlet 2, closest to the ideal calibration, occurs when outlet tube 2 is positioned between the two inlets (i.e., $0.250 < \alpha < 0.750$). Conversely, at the extreme positions, with α equal to 0.150 and 0.850, the values do not converge toward the optimal condition. Furthermore, analysis of the curves for the different outlet diameter ratios indicates that when the velocity ratio ψ equals 0.60, the highest particle concentration occurs at a diameter ratio of 0.60. This behavior arises because a smaller outlet diameter results in a longer tube length, under the study's assumption of a constant-volume geometry. Accordingly, analysis of the 240 obtained results showed that only three points exhibit errors of up to 10% relative to the ideal calibration value of 50%.

Among the combinations of degrees of freedom, one configuration exceptionally close to the optimal target value ($\beta^*_{(2,2)}$) is identified for $\psi = 1.20$, with α and aD values of 0.675 and 0.60, respectively. In addition, two optimized points are observed for $\psi = 1.00$, occurring at $\alpha = 0.325$ for aD = 1.00 and 0.60, respectively, as summarized in Table 6. To ensure the robustness of the optimal configurations identified in this table, a high-

resolution validation was performed. The three optimized cases were resimulated with a finer spatial discretization (medium mesh) and a refined temporal resolution (time step of 0.01 s). The high-resolution results yielded particle concentrations at outlet 2 of 49.39%, 51.43%, and 49.81%, respectively. The minimal deviation from the initial parametric sweep confirms that the identified optimal points reflect physical flow behavior rather than numerical artifacts arising from spatial or temporal discretization limits.

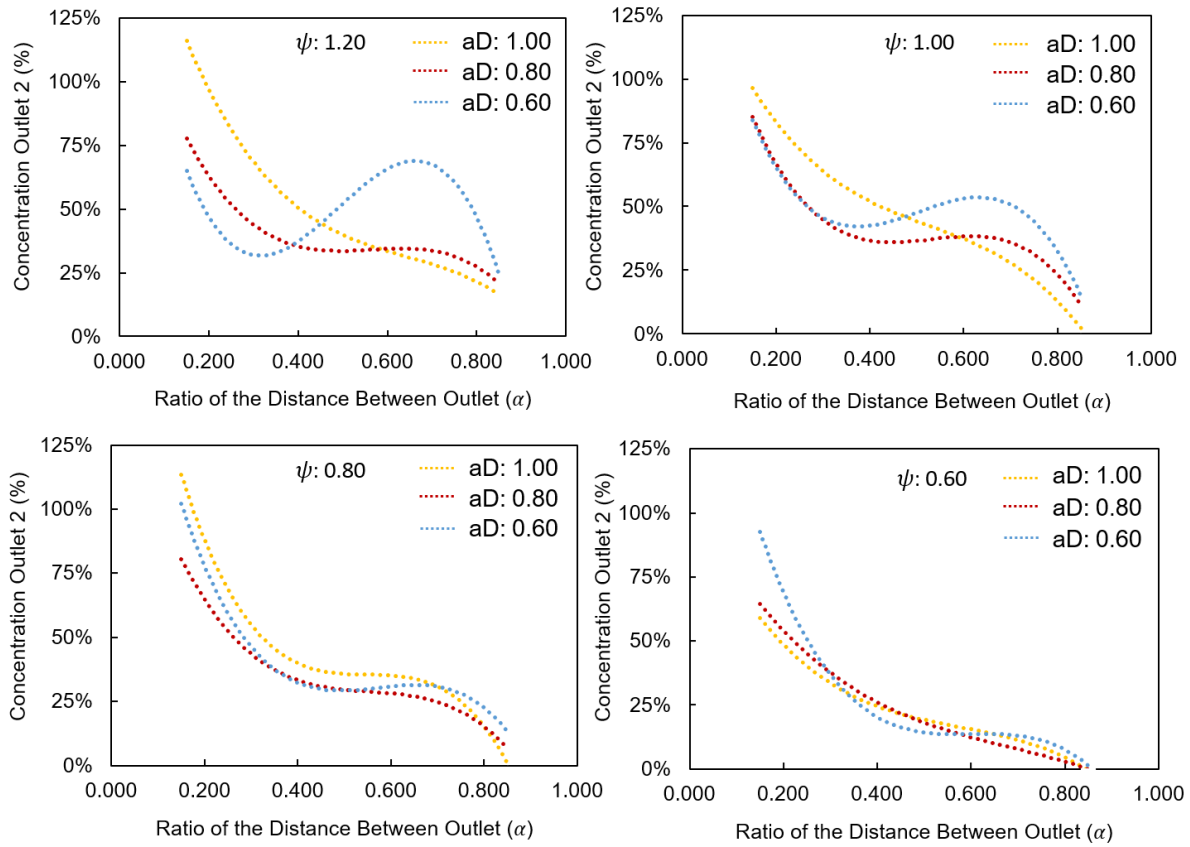

Figure 7. Particle concentration at outlet 2 as a function of the vertical position (α) and diameter ratio (aD) for the four evaluated inlet velocity ratios (ψ) at D_0 = 2.00 mm.

Table 6. The particle concentration values measured at outlet 2 approximate the optimal value.

ψ	α	aD	$\beta^*_{(2,2)}$ (%)	Element Size 0.1425 mm Time-Step 0.05 s		Element Size 0.1089 mm Time-Step 0.01 s	
				$\beta_{(2,2)}$ (%)	ε (%)	$\beta_{(2,2)}$ (%)	ε (%)
1.00	0.325	0.60	50.00	47.31	5.38	49.39	1.23
1.00	0.325	1.00	50.00	53.68	7.36	51.43	2.86
1.20	0.675	0.60	50.00	47.59	4.82	49.81	0.39

Figure 8 shows particle concentration contours in terms of mass per unit volume. The results show that reducing the outlet diameter (aD = 0.60) decreases the particle concentration at the lateral outlets. This behavior occurs because reducing the diameter ratio under a constant-volume constraint requires a proportional increase in tube length, thereby elevating the system's frictional losses and overall flow resistance. This characteristic has also been reported in Y-shaped or dendritic flow networks, where the diameter ratio aD controls the network's hydraulic resistance. In these systems, smaller diameter ratios increase friction losses due to the longer tubes required by the constant-volume constraint, while larger diameters tend to reduce the overall flow resistance [29,33]. Furthermore, as outlet tube 2 moves farther away from inlet 1, the location where particles enter the

system, the particle concentration in the flow decreases. This trend is consistent with the behavior previously observed in Figure 7.

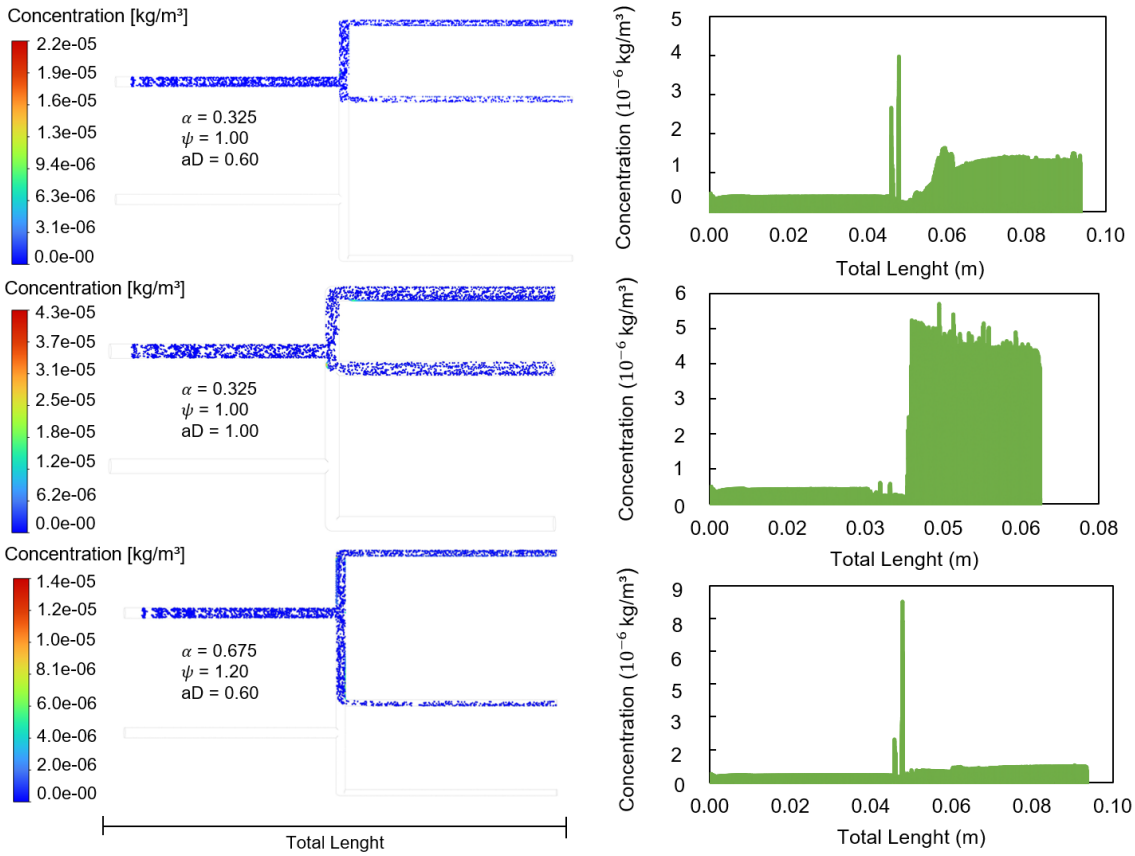

Figure 8. Spatial concentration contours (**left**) and longitudinal concentration profiles (**right**) demonstrating the fluid-particle distribution for the three optimized geometric configurations identified in Table 6.

3.3. FPR Analysis Based on the Application of Degrees of Freedom

Figures 9–11 show the Flow Partition Ratio (FPR) for each outlet in the analyzed configuration, considering each combination of inlet velocity ratio ψ and the vertical position α. These figures illustrate the flow-rate behavior resulting from the degrees of freedom adopted in the study, with each graph corresponding to a different inlet velocity ratio.

The FPR analysis shows that even in geometrically symmetric configurations, the flow does not always distribute uniformly across the device's branches. This behavior indicates that geometric and hydrodynamic factors directly influence the flow partition [29,32,33].

The results indicate that the flow distribution depends significantly on the geometric characteristics of the network, including the diameter ratio (aD), the position of outlet tube 2 along the structure, and the system slenderness. This occurs because maintaining a constant total volume requires that variations in diameter be compensated by changes in tube length. The results show that at the minimum evaluated vertical position ($\alpha = 0.150$), the flow rate at outlet 3 tends to be highest. Conversely, at the maximum evaluated position ($\alpha = 0.850$), the flow rate at outlet 1 increases.

Furthermore, changes in geometric parameters can make the flow distribution more or less homogeneous, as reported in previous studies [29,33]. Under certain conditions, reducing the diameter ratio promotes a more uniform flow distribution among the network's branches. Therefore, the FPR is an important tool for evaluating the hydraulic performance of branched networks and for understanding how geometry influences flow distribution.

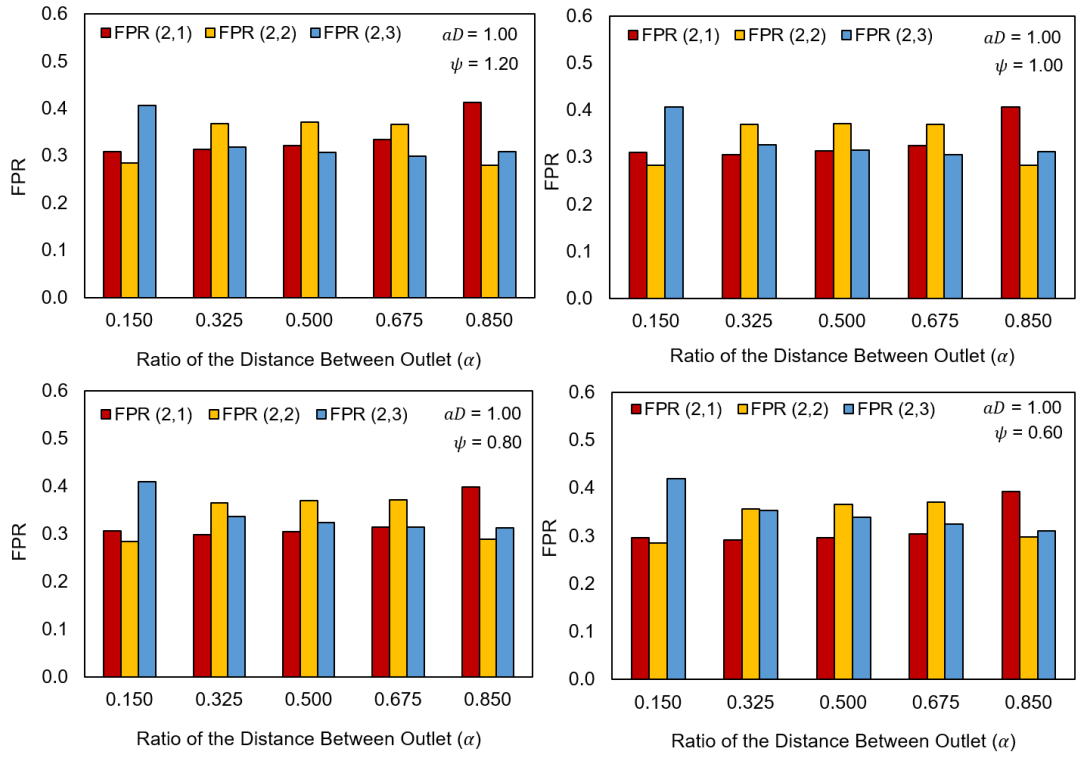

Figure 9. Flow Partition Ratio (FPR) distribution among the three outlets for a diameter ratio aD equal to 1.00. The subplots illustrate the distribution across multiple vertical positions (α) for the four evaluated inlet velocity ratios (ψ).

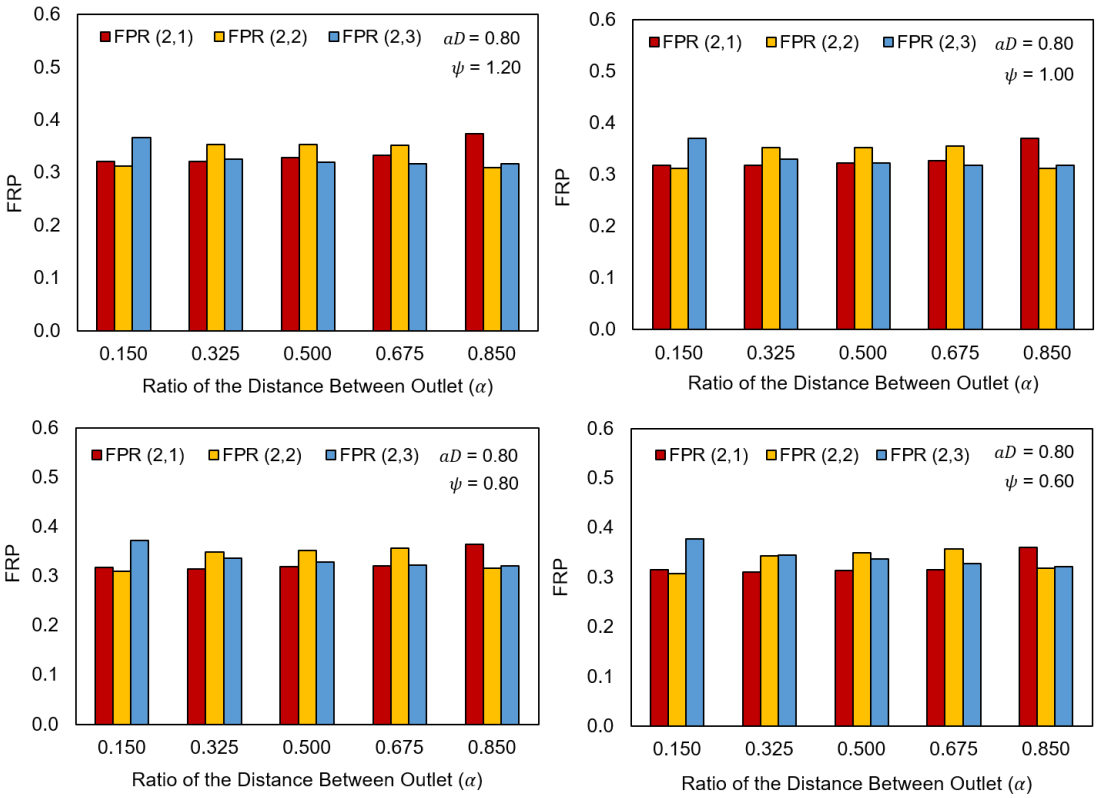

Figure 10. Flow Partition Ratio (FPR) distribution among the three outlets for a diameter ratio aD equal to 0.80. The subplots illustrate the distribution across multiple vertical positions (α) for the four evaluated inlet velocity ratios (ψ).

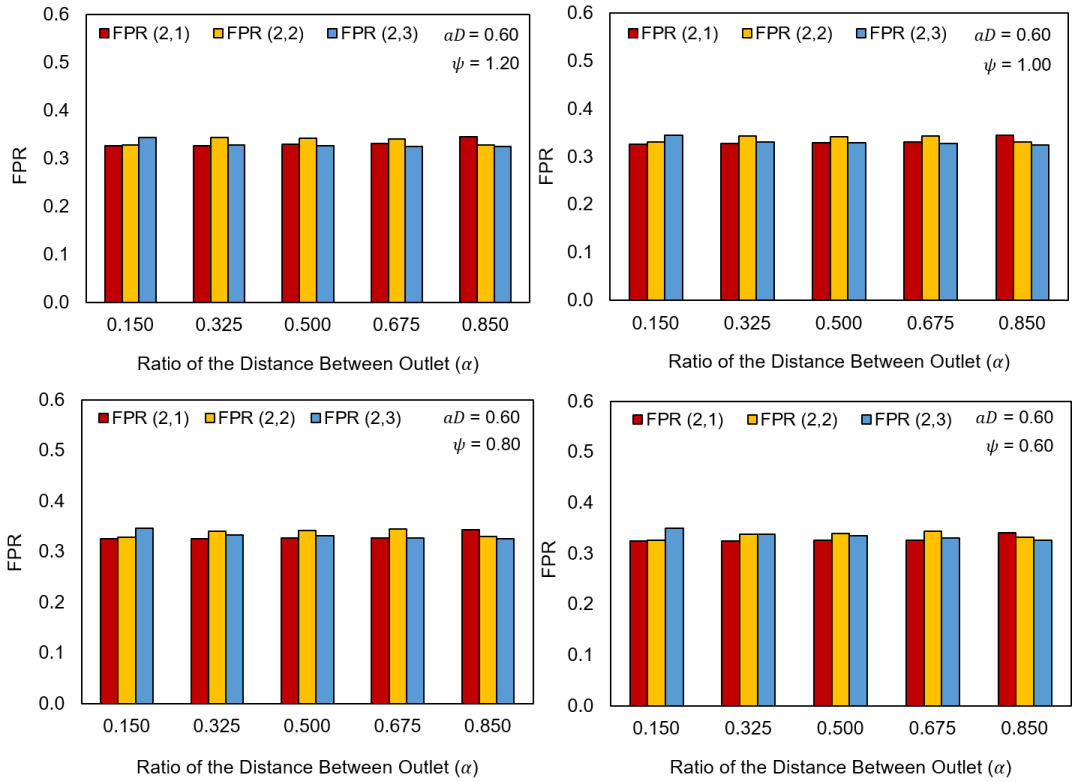

Figure 11. Flow Partition Ratio (FPR) distribution among the three outlets for a diameter ratio aD equal to 0.60. The subplots illustrate the distribution across multiple vertical positions (α) for the four evaluated inlet velocity ratios (ψ).

3.4. Flow Resistance Analysis Based on the Application of Degrees of Freedom

Figure 12 shows the behavior of the flow resistance as a function of the variation in the vertical position of outlet tube 2 (α), the inlet velocity ratio represented by the parameter (ψ), and the diameter ratio (aD). The results show that increasing the inlet velocity ratio (ψ), which corresponds to increasing the absolute flow velocity at inlet 1 relative to inlet 2, results in higher flow resistance. This indicates a direct relationship between higher fluid velocity and greater hydraulic losses within the system. This behavior is consistent with results reported in the literature, which show that increasing flow conditions intensify inertial effects and pressure losses throughout the network, thereby increasing flow resistance [29,32,33].

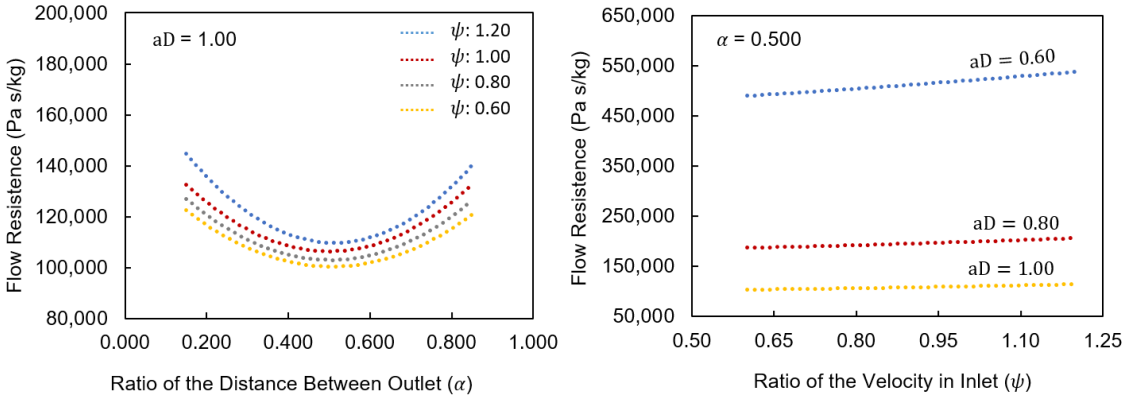

Figure 12. Flow resistance behavior across the evaluated degrees of freedom. The (**left**) graph illustrates resistance as a function of the vertical position (α) for a constant diameter ratio (aD = 1.00). The (**right**) graph demonstrates resistance as a function of the inlet velocity ratio (ψ) across different diameter ratios (aD) for a symmetric position (α = 0.500).

In addition, variations in the outlet tube diameter strongly influence flow resistance. Lower values of the diameter ratio, such as aD = 0.60, produce significantly higher resistance than aD = 0.80 or 1.00, indicating that reducing the diameter increases friction losses and the pressure drop in the system [29,32,33]. Furthermore, the geometric asymmetry introduced by the variation in the vertical position of outlet tube 2 also modifies the flow distribution and the pressure losses along the device, directly influencing the resistance values obtained.

3.5. Analysis of Velocity and Pressure Contours

Figure 13 shows the static pressure contours and the corresponding pressure profiles along the device's total length for three vertical positions of outlet tube 2. In all cases, the pressure gradually decreases along the flow path due to head losses associated with wall friction and geometric singularities at the system's bifurcation. However, the system exhibits higher pressure and greater flow resistance when outlet tubes 1 and 2 are positioned closer together, as in the case of $\alpha = 0.150$. In this configuration, the proximity of the branches intensifies localized losses in the flow-division region, thereby increasing energy dissipation. In contrast, when the tubes are arranged in a more symmetric configuration ($\alpha = 0.500$), the system presents a more uniform pressure distribution and smaller pressure gradients near the bifurcation. This condition reduces the hydraulic resistance and localized pressure losses, thereby allowing the fluid to flow more freely through the device. In addition to the geometric influence of outlet position, tube diameter variation also plays a significant role in flow resistance, as shown in Figure 14. Smaller values of the diameter ratio (aD = 0.60) increase the pressure at the inlet region of the system. This behavior occurs because a reduction in the flow area increases the system's hydraulic resistance, thereby requiring a larger pressure gradient to maintain the same flow rate [29,33]. As a result, the fluid exhibits higher upstream pressure and a more pronounced pressure drop along the device. Similarly, increasing the inlet velocity ratio (ψ) raises the system pressure. Thus, the behavior observed in the figures indicates that the device's hydraulic resistance arises from the interaction between geometric parameters, such as the positions and diameters of the outlet tubes, and operational parameters, such as the inlet flow velocity [29,32,33].

Figure 15 shows the velocity magnitude contours and the velocity profiles along the total length of the device for different vertical positions of outlet tube 2. Initially, the velocity gradually increases along the inlet channel, a behavior associated with flow development and the evolution of the boundary layer along the tube walls. As the fluid approaches the bifurcation region, the velocity magnitude changes abruptly, as highlighted by the peak observed in the velocity profiles. The contraction of the streamlines and the redistribution of the flow between the system branches cause this behavior.

After the flow division region, the mean velocity decreases, and small oscillations appear in the velocity profiles. These features indicate hydrodynamic effects associated with boundary-layer separation and the formation of recirculation regions near the inner walls of the bifurcation. In addition, the vertical position of outlet tube 2 influences the intensity of these variations. When the system approaches a more symmetric configuration ($\alpha = 0.500$), the velocity profiles become smoother and more uniform along the branches, indicating a more balanced redistribution of the flow and fewer hydrodynamic disturbances in the flow division region. In contrast, more asymmetric configurations intensify velocity gradients and promote the development of localized separation regions.

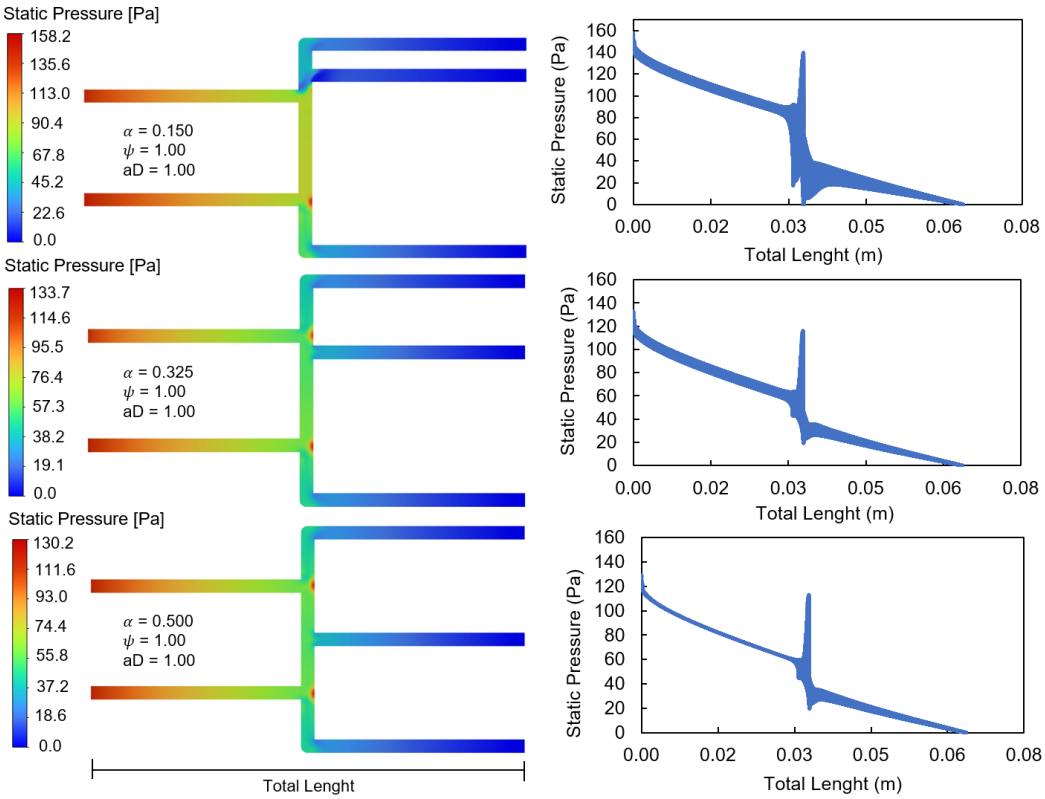

Figure 13. Static pressure contours (**left**) and longitudinal profiles (**right**) for a geometry aD = 1.00 and ψ = 1.00 across different vertical positions (α).

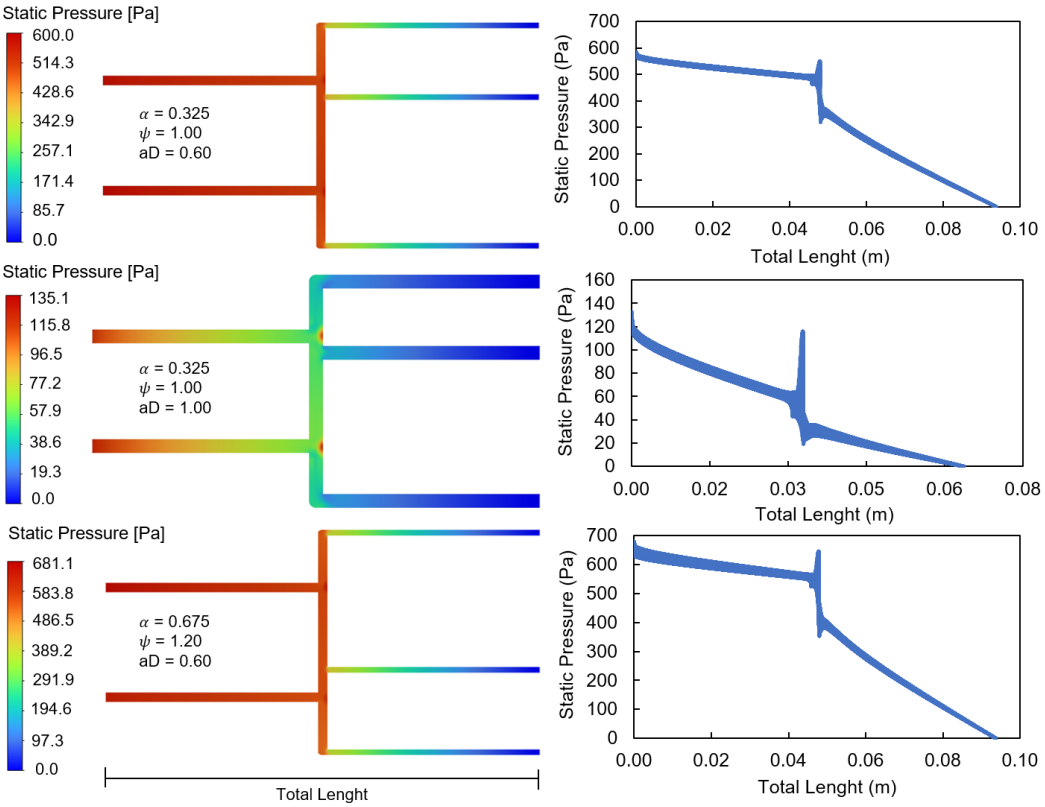

Figure 14. Static pressure contours (**left**) and longitudinal profiles (**right**) for geometries corresponding to the optimized configurations identified in Table 6.

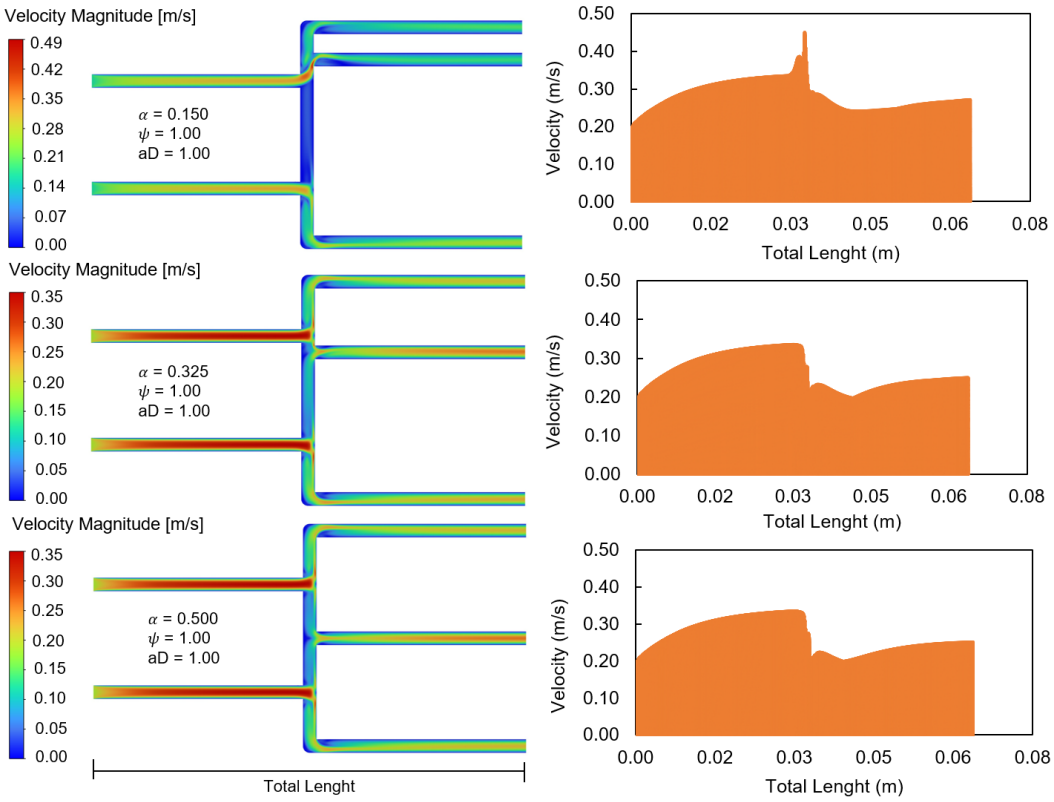

Figure 15. Velocity magnitude contours (**left**) and longitudinal profiles (**right**) for a geometry with aD = 1.0 and ψ = 1.0 across different vertical positions (α).

Regarding the geometries that present values close to the optimal condition (Table 6), that is, those that exhibit particle percentages of 100%, 50%, and 0% at outlets 1, 2, and 3, respectively, we observe an increase in the flow velocity inside the outlet tubes when the diameter ratio is aD = 0.60. This behavior occurs because flow velocity is directly related to the Reynolds number and the channel diameter; therefore, higher Reynolds numbers and smaller diameters lead to higher flow velocities.

By analyzing Figure 16, we observe that the outlet velocities are approximately twice as high for geometries with a diameter ratio aD = 0.60. This result is associated with a reduction in the cross-sectional area available for flow, which increases the mean fluid velocity to conserve the mass flow rate within the system. Furthermore, geometric changes in the bifurcation regions, particularly near the junctions between the vertical and outlet tubes, can generate local redistributions of the velocity field. This includes the induction of low-intensity recirculation regions near the walls and the temporary displacement of the hydrodynamic boundary layer. Reducing the tube diameter further increases the velocity gradient near the walls, thereby intensifying boundary layer growth. Finally, these localized effects contribute to the reorganization of the flow and the emergence of small local asymmetries, all without compromising the overall stability of the laminar flow regime. Notice that, despite the presence of localized velocity redistributions and minor recirculation zones at the bifurcations, no significant particle deposition or permanent trapping was observed in the simulations. Because the microbubbles possess an extremely low Stokes number, their inertia is negligible, ensuring they remain firmly entrained within the bulk fluid streamlines rather than migrating toward the walls at sharp turns. Furthermore, the numerical model assumes non-adherent (reflective) wall boundary conditions for the discrete phase, which reflect the physical behavior of stabilized, lipid-shelled contrast agents that resist adhesion in smooth calibration manifolds.

Consequently, the microbubbles are efficiently transported through the junctions without accumulating in the localized dead zones.

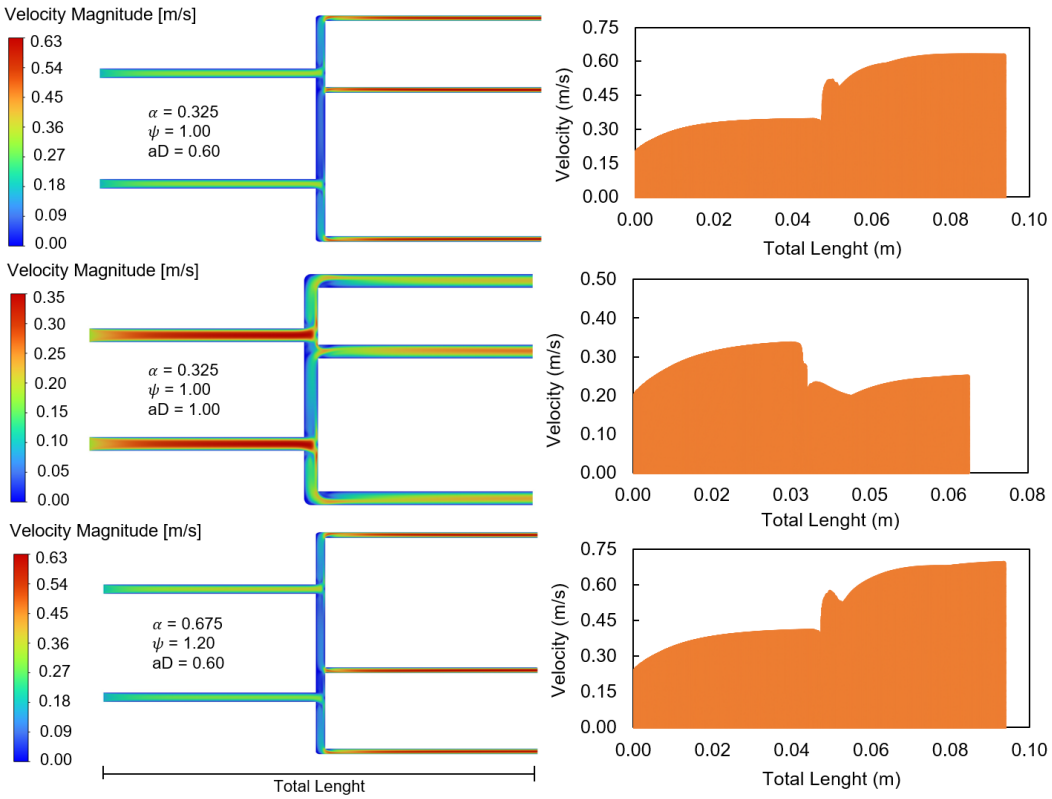

Figure 16. Velocity magnitude contours (**left**) and longitudinal profiles (**right**) for geometries corresponding to the optimized configurations identified in Table 6.

3.6. Analysis of the Influence of Inlet Tube Variation on Flow and Concentration Behavior

To evaluate the behavior of particle concentration in the flow, the degree of freedom associated with the vertical position of the inlet tubes (δ) was analyzed. Four distinct configurations were considered: approximation between the inlet tubes (δ = 0.150), positioning them closer to outlet 2; separation between the inlet tubes (δ = 0.850), bringing them closer to outlets 1 and 3, respectively; and two intermediate configurations in which the tubes maintain a constant relative distance while being vertically shifted together upward (δ = 0.250) and downward (δ = 0.750).

Figure 17 shows the distribution of particle concentration and FPR for these configurations, considering two diameter ratios (aD = 1.00 and aD = 0.60). The analysis of the results indicates that, for the condition in which the inlet tubes are close to each other (δ = 0.150), the concentration distribution at the outlets shows low sensitivity to variations in aD, with nearly overlapping behavior across the analyzed cases. In this configuration, a significant reduction in particle concentration is observed at outlet 2, reaching values close to 24%, which deviates from the ideal concentration behavior, i.e., 50% of particles at outlet 2. On the other hand, for the condition of greater separation between the tubes (δ = 0.850), there is an increase in particle concentration at the lateral outlets, associated with the redistribution of streamlines and reduced interaction between the two inlet flows. In this case, increasing the diameter ratio slightly intensifies this trend, suggesting that geometry influences momentum dissipation and convective particle transport. For the intermediate configurations (δ = 0.250 and δ = 0.750), similar behavior is observed, with concentration profiles showing little sensitivity to variations in aD. This indicates that, under

these conditions, the flow exhibits a more stable mixing regime, in which the symmetric distribution of the inlet streams partially compensates for geometric effects.

Regarding the FPR, increasing the distance between the inlet tubes relative to the central outlet (δ = 0.850) yields more homogeneous outlet values, indicating a more balanced phase distribution. This behavior can be explained by reduced direct interaction between the inlet jets, which favors a more distributed flow regime with less pronounced regions of high concentration.

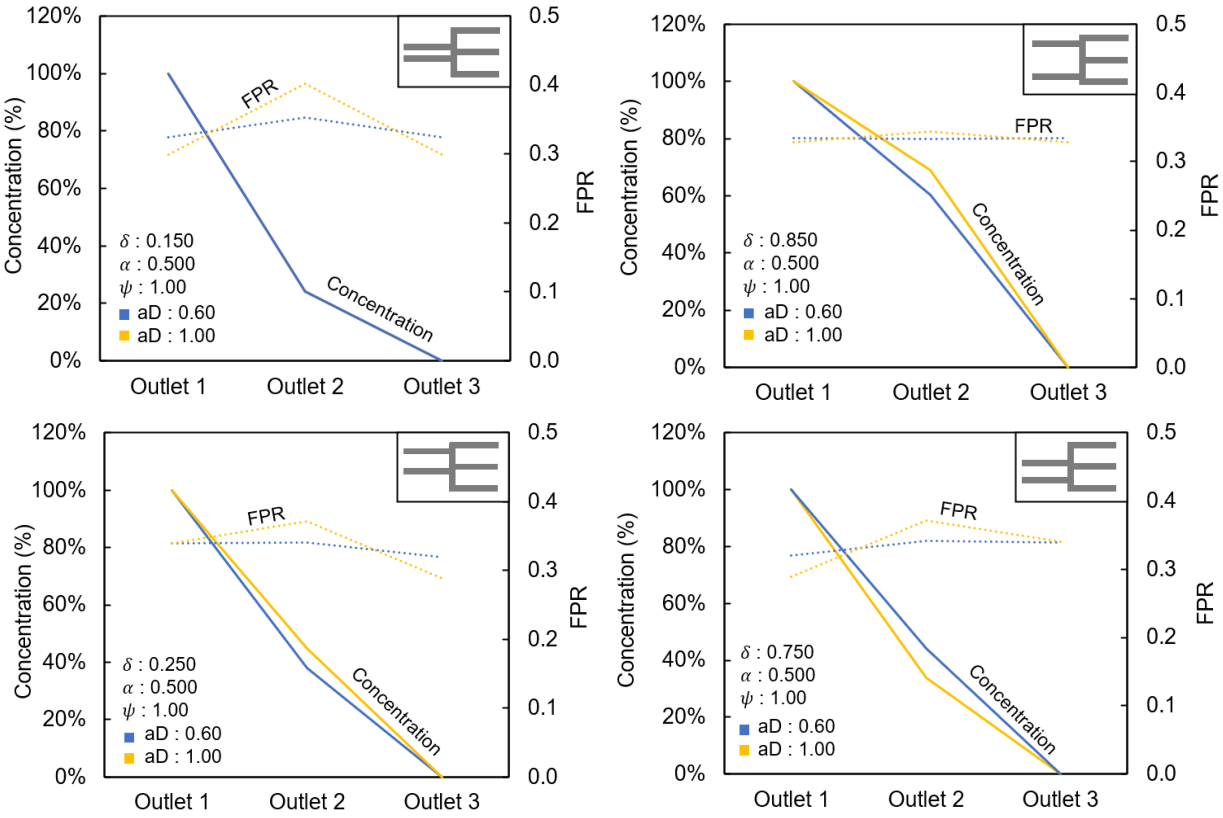

Figure 17. Particle concentration and Flow Partition Ratio (FPR) distributions across the three outlets for varying vertical positions of the inlet tubes (δ). The analysis compares diameter ratios aD = 1.00 and aD = 0.60, while maintaining a constant inlet velocity ratio (ψ = 1.00) and a symmetric outlet position (α = 0.500).

3.7. Analysis of Intermediate Concentration Levels Based on the Application of Degrees of Freedom

The present study aims to determine which configuration, when degrees of freedom are applied, yields the concentration divider–based device a response closest to linearity for particle concentrations of 100%, 50%, and 0% at outlets 1, 2, and 3, respectively. However, after compiling the results, other possible applications were identified, including different intermediate particle concentrations. Thus, Figures 18–20 present the variation in particle concentration for combinations of the degrees of freedom (ψ, α, and aD), assuming symmetric inlet tube positions. Furthermore, Figure 21 presents six distinct cases in which the relationship between particle concentration and FPR can be analyzed at intermediate concentrations, and these results may be applied to other purposes.

The concentration distribution among the outlets is influenced by both the diameter ratio (aD) and the vertical position ratio of outlet 2 (α). In general, outlet 1 shows the highest particle concentrations because it is more directly aligned with the particle inlet flow. However, when aD = 1.00 and outlet 2 is positioned closer to outlet 1 (α = 0.150), the

concentration at outlet 2 may exceed that of outlet 1. This occurs because the particle-laden flow reaches outlet 2 before outlet 1, increasing the particle concentration at this intermediate outlet. Conversely, for $\alpha = 0.850$, the concentration at outlet 3 becomes non-negligible and may even surpass that of outlet 2, due to the greater distance between outlet 2 and the particle inlet.

Additionally, reducing the diameter ratio (aD = 0.80 and 0.60) enhances flow separation, promoting a more gradual redistribution of particles among the outlets. Under these conditions, outlet 2 becomes more sensitive to variations in α, while outlet 3 maintains lower, though not necessarily negligible, concentrations depending on the geometric configuration.

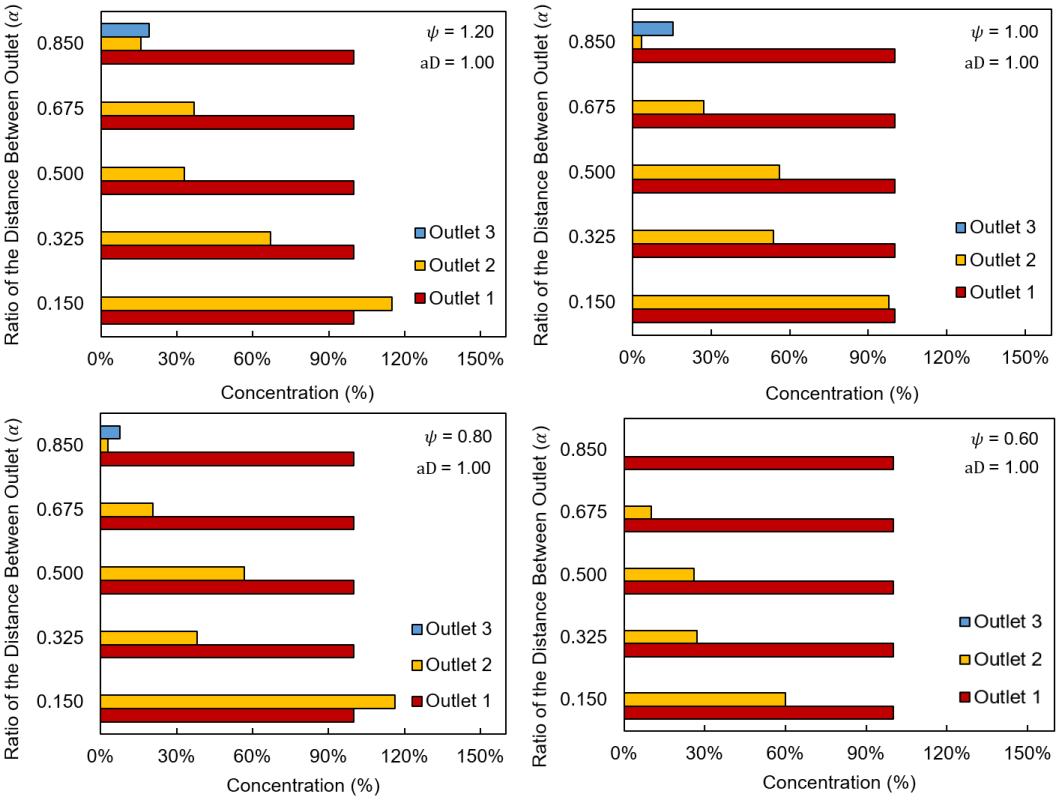

Figure 18. Particle concentration distributions across the three outlets for varying vertical positions (α) and inlet velocity ratios (ψ) at a constant diameter ratio of aD = 1.00.

To analyze particle concentration and FPR behavior, Figure 21 presents six distinct cases with different particle distributions and corresponding FPR values at outlets 1, 2, and 3. For $\alpha = 0.150$, the particle concentration decreases at outlets 1 and 2, while increasing at outlet 3, despite the higher fluid flow fraction directed to that outlet. This behavior is driven by the kinematic routing of the fluid stream surfaces rather than inertial particle separation. Because the contrast agent microbubbles are exceptionally small (3 μm) and the flow is laminar, the particles possess a very low Stokes number. Thus, particle inertia is negligible, and the discrete phase faithfully follows the continuous phase streamlines. Therefore, the mechanism affecting the concentration gradient is the shifting of the dividing stream surfaces (the internal topological boundaries within the bifurcation that dictate which outlet a fluid parcel will enter).

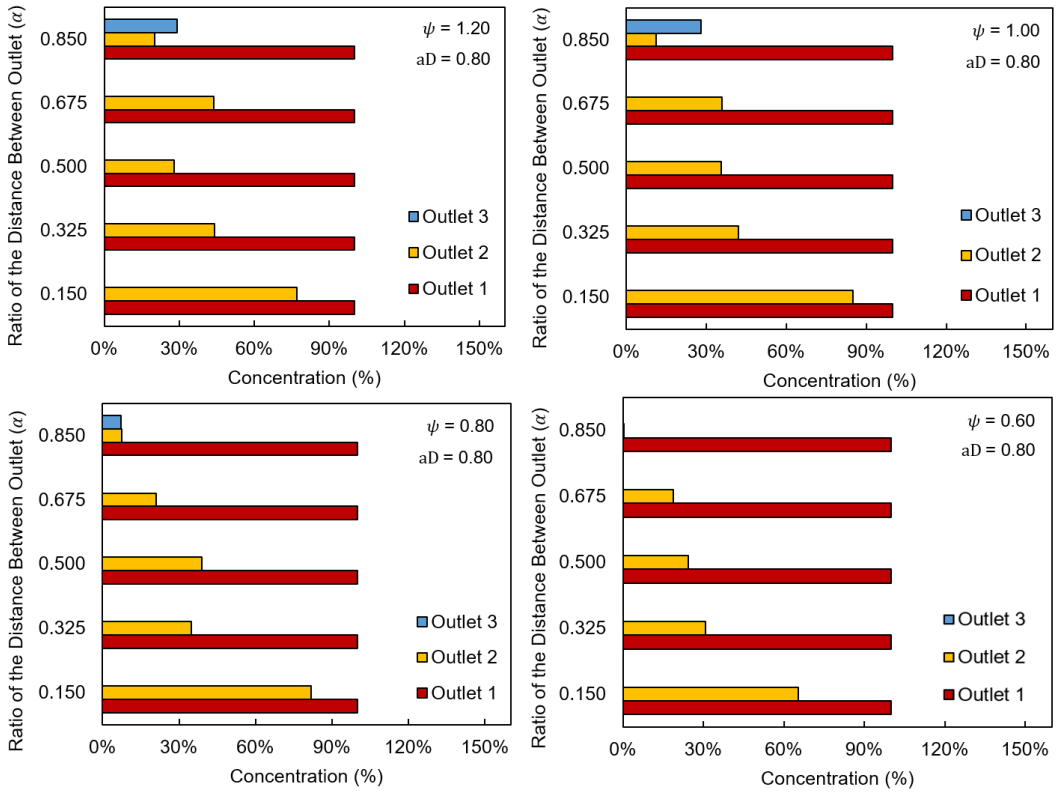

Figure 19. Particle concentration distributions across the three outlets for varying vertical positions (α) and inlet velocity ratios (ψ) at a constant diameter ratio of aD = 0.80.

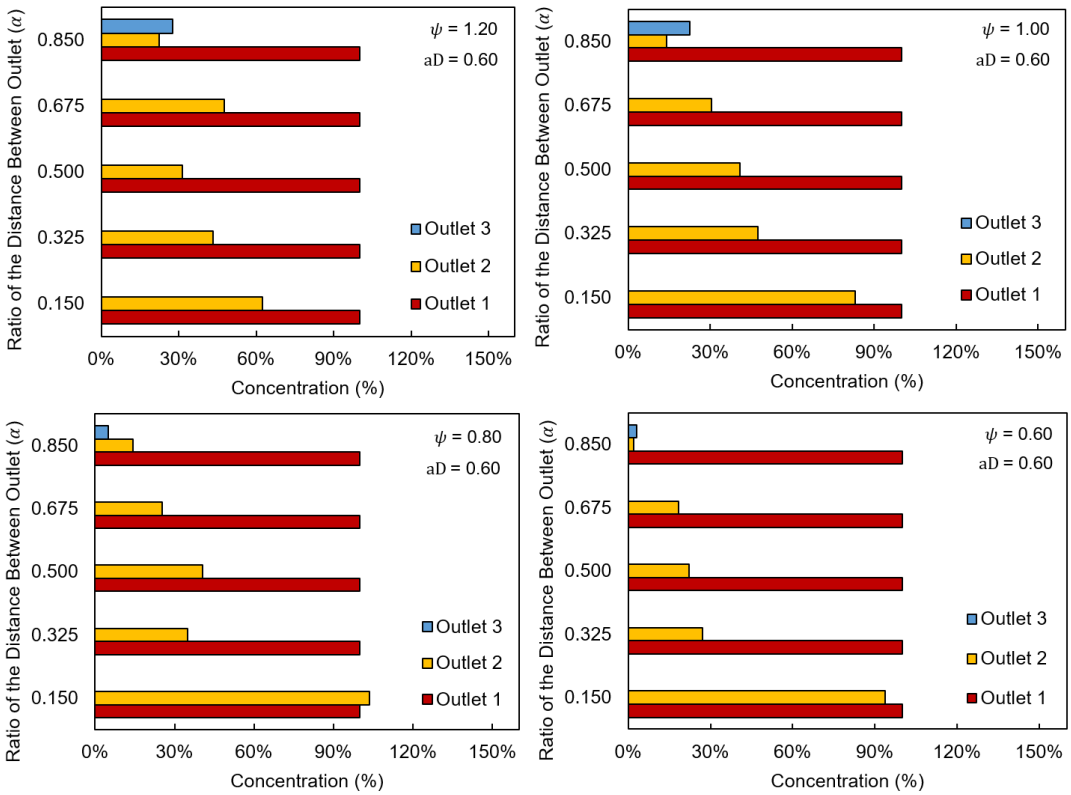

Figure 20. Particle concentration distributions across the three outlets for varying vertical positions (α) and inlet velocity ratios (ψ) at a constant diameter ratio of aD = 0.60.

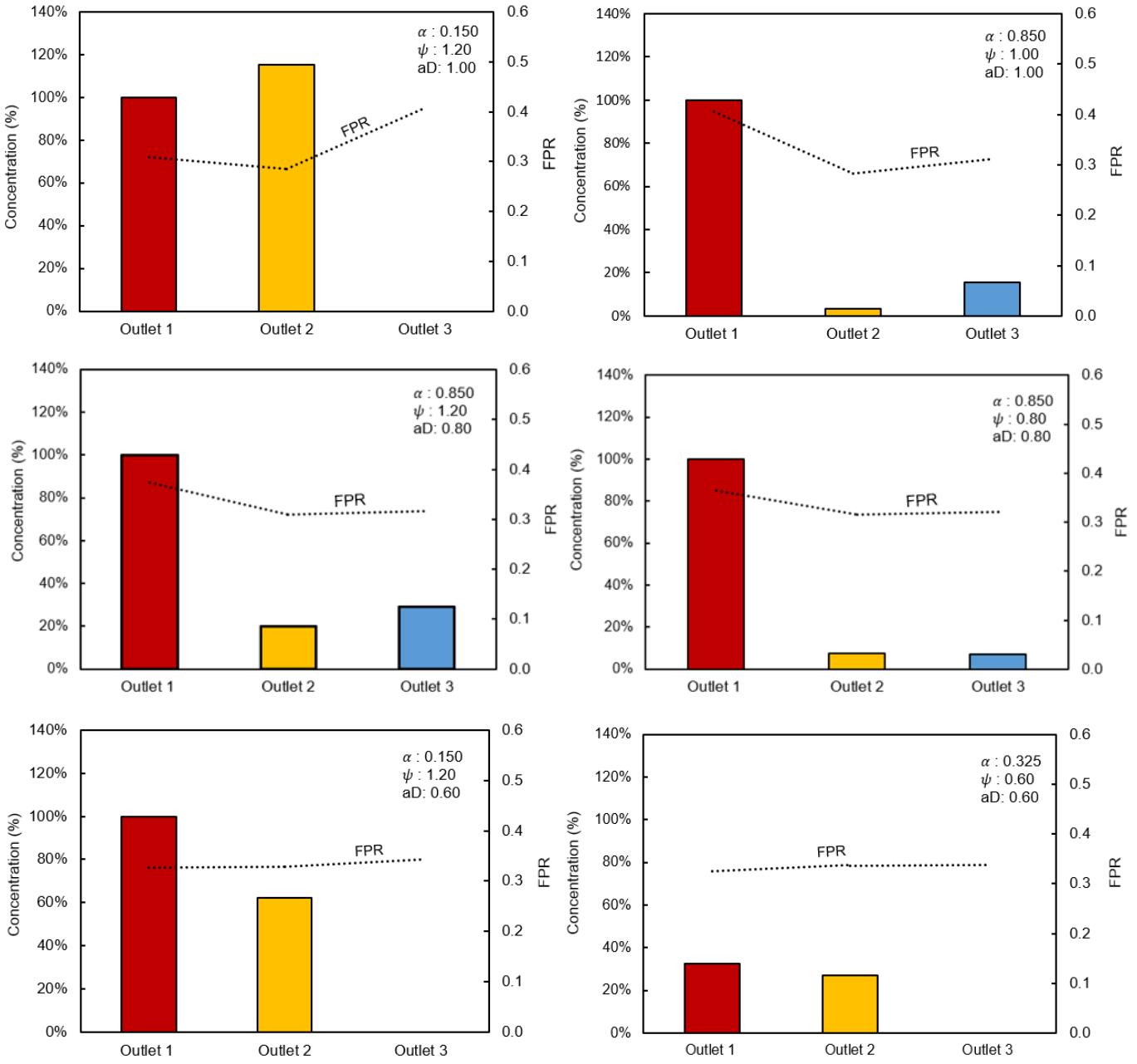

Figure 21. Comparative analysis of Particle Concentration (solid lines) and Flow Partition Ratio (FPR, dotted lines) across the three outlets for six selected intermediate device configurations.

When the geometry is modified (e.g., by shifting the vertical position of outlet 2), the stagnation points inside the junction relocate, fundamentally altering how the specific fluid layer originating from inlet 1 is sliced and routed. Consequently, the concentration at any given outlet is a direct macroscopic reflection of how the geometry controls the dividing stream surfaces of the particle-laden layer. Furthermore, reducing the diameter ratio to aD = 0.60 promotes a more uniform flow distribution among the outlets.

The results also show that the fluid flow partition ratio (FPR) does not directly determine the particle concentration distribution within the device. Although outlet 3 receives a significant portion of the continuous phase flow, the particle concentration remains preferentially distributed toward outlets 1 and 2. This behavior highlights the importance of three-dimensional flow structures and streamline redistribution, suggesting that simplified one-dimensional hydraulic approaches may not accurately predict particle transport in DCE-US calibration devices.

4. Conclusions

This study presented a numerical investigation of a concentration divider for calibrating dynamic contrast-enhanced ultrasound (DCE-US) devices using the Constructal Design method. By varying the geometric (aD, α, and δ) and operational (ψ) degrees of freedom while keeping the inlet diameter and the total device volume constant, it was possible to identify configurations capable of promoting a more linear and uniform particle concentration distribution at the system outlets.

The results demonstrated that geometric symmetry plays a fundamental role in achieving optimal calibration conditions. Configurations in which outlet tube 2 is positioned close to the symmetry plane (α = 0.325 and α = 0.500), combined with equal inlet velocities (ψ = 1.00), produced particle concentrations at outlet 2 close to the ideal value of 50%. This behavior indicates that the performance of the concentration divider depends mainly on the geometric position of outlet tube 2 and on the flow conditions.

In addition, the diameter ratio proved to be a relevant parameter influencing flow resistance and particle distribution. Although reducing the outlet diameter (aD = 0.60) increased hydraulic resistance and pressure levels due to the longer channel lengths imposed by the constant-volume constraint, this configuration also resulted in higher outlet flow velocities. Furthermore, all optimized configurations remained within the laminar flow regime, ensuring stable, predictable flow, which is essential for calibration applications.

The FPR analysis indicated that configurations close to symmetry favor a more uniform distribution of mass flow rate among the device outlets. The pressure and velocity field analyses also showed that intermediate values of α reduce localized pressure losses and promote a more balanced redistribution of flow within the system.

Overall, the application of the Constructal Design method proved an effective approach for guiding the geometric optimization of concentration dividers for the calibration of ultrasound systems. The identified configurations strike a favorable balance among concentration linearity, flow uniformity, and hydraulic efficiency, enabling more accurate and cost-effective calibration of DCE-US systems. By improving control over the distribution of contrast agent particles, the proposed approach directly contributes to increased diagnostic reliability and to the rational development of microfluidic devices at the interface between engineering and medical imaging.

Furthermore, it was observed that the device does not require a linear response with fixed concentrations at the outlets. The results also demonstrated the possibility of obtaining intermediate particle concentrations, which may be explored for other applications. In this context, the same study, based on the Constructal Design method, can also be extended to mixing devices, since variations in geometric and operational degrees of freedom enable the achievement of different concentration distributions. These intermediate results are advantageous for applications requiring precise concentration control, thereby expanding the device's versatility and potential applicability in microfluidic systems, mixing processes, and other engineering and biomedical applications.

An important finding of the present study is that the fluid flow partition ratio (FPR) alone is insufficient to predict particle concentration redistribution within the concentration divider. The results demonstrated that particle transport behavior is strongly influenced by three-dimensional streamline organization and local bifurcation effects, leading to concentration distributions that do not necessarily follow the continuous-phase flow distribution. This observation underscores the importance of using three-dimensional CFD simulations coupled with the Discrete Phase Model (DPM), as simplified one-dimensional hydraulic models may not adequately capture the complex phase redistribution mechanisms in DCE-US calibration systems.

Based on the obtained results, the main conclusions of this study can be summarized in the following points:

- Symmetry drives optimal calibration: The geometric symmetry of the device is the most critical factor for achieving an adequate distribution of particle concentration. Positioning outlet tube 2 near the symmetry plane (α = 0.325 to 0.500), combined with equal inlet velocities (ψ = 1.00), consistently provided particle concentrations at outlet 2 closest to the ideal 50% target.
- Diameter ratios dictate a hydraulic tradeoff: The diameter ratio (aD) directly influences flow resistance. While reducing the outlet diameter (aD = 0.60) increased outlet flow velocity, it also increased hydraulic resistance and pressure losses due to the longer channel lengths required by the constant-volume constraint.
- Flow distribution is highly sensitive to geometry: The Flow Partition Ratio (FPR) analysis demonstrated that even small geometric asymmetries significantly alter flow distribution. Intermediate values of α were shown to reduce localized pressure losses and promote a more balanced redistribution of flow within the system.
- Laminar stability is maintained: Across all optimized configurations, the flow remained within the laminar regime, ensuring the stable and predictable flow behavior that is essential for accurate calibration applications.

Upcoming Studies

Regarding future studies, we are advancing this research to expand the analysis of geometric degrees of freedom and investigate the effects of asymmetries introduced into originally symmetric structures. Planned investigations include:

- Applying two additional degrees of freedom related to tube length ratios (Li/Lj), specifically considering: (i) variations in the length of the inlet tubes relative to the vertical tube, and (ii) variations in the length of the vertical tube relative to the outlet tubes.
- Exploring further degrees of freedom related to tube diameter ratios (Di/Dj) to more comprehensively evaluate their influence on hydraulic performance and particle distribution.
- Analyzing different volume fractions within the device to identify how the total volume allocation affects the calibration process and overall flow dynamics.
- Expanding the number of branching stages in the calibration device to evaluate system behavior, scalability, and optimization potential under more complex geometric configurations.

Author Contributions: Conceptualization, A.F.M. and L.A.O.R.; methodology, V.R.P.; software, K.V.M. and F.H.; validation, K.V.M.; formal analysis, K.V.M., V.R.P. and A.F.M.; investigation, K.V.M., V.R.P. and A.F.M.; data curation, K.V.M.; writing—original draft preparation, K.V.M., F.H., V.R.P., A.F.M., F.S.F.Z. and L.A.O.R.; writing—review and editing, K.V.M., F.H., V.R.P., A.F.M., F.S.F.Z. and L.A.O.R.; supervision, A.F.M. and L.A.O.R. All authors have read and agreed to the published version of the manuscript.

Funding: This study was financed by the Coordination for the Improvement of Higher Education Personnel (CAPES/Brazil—Finance Code 001). Machado, K.V. is a grant holder CAPES (Process: 88887.972193/2024-00). Haeberle, F. is a grant holder CNPq (Process: 141554/2024-0). Rocha, L.A.O., is a grant holder PQ CNPq (Process 307038/2025-4). Zinani. F.S.F is a grant holder PQ CNPq (Proc. No. 304832/2025-1 and 201546/2025-6). Complex Flow Systems Lab researchers acknowledge the financial support provided to the Institute of Earth Sciences (ICT) through the multi-annual funding contract with the Foundation for Science and Technology (FCT), under project UID/0468.

Data Availability Statement: Data will be made available on request.

Conflicts of Interest: The authors declare that they have no known competing financial interests or personal relationships that could have appeared to influence the work reported in this paper.

Abbreviations

DCE-US	Dynamic Contrast-Enhanced Ultrasound
CFD	Computational Fluid Dynamics
DPM	Discrete Phase Model
GCI	Grid Convergence Index
FPR	Flow Partition Ratio

References

1. Gramiak, R.; Shah, P.M. Echocardiography of the aortic root. *Investig. Radiol.* **1968**, *3*, 356–366. https://doi.org/10.1097/00004424-196809000-00011.
2. Kremkau, F.W.; Gramiak, R.; Carstensen, E.L.; Shah, P.M.; Kramer, D.H. Ultrasonic detection of cavitation at catheter tips. *Am. J. Roentgenol.* **1968**, *3*, 159–167.
3. Kremkau, F.W.; Gramiak, R.; Carstensen, E.L.; Shah, P.M.; Kramer, D.H. Ultrasonic detection of cavitation at catheter tips. *Am. J. Roentgenol.* **1970**, *110*, 177–183. https://doi.org/10.2214/ajr.110.1.177.
4. Schneider, M.; Arditi, M.; Barrau, M.B.; Brochot, J.; Broillet, A.; Ventrone, R.; Yan, F. BR1: A new ultrasonographic contrast agent based on sulfur hexafluoride-filled microbubbles. *Investig. Radiol.* **1995**, *30*, 451–457. https://doi.org/10.1097/00004424-199508000-00001.
5. Zavariz, J.D.; Konstantatou, E.; Deganello, A.; Bosanac, D.; Huang, D.Y.; Sellars, M.E.; Sidhu, P.S. Common and uncommon features of focal splenic lesions on contrast-enhanced ultrasound: A pictorial review. *Radiol. Bras.* **2017**, *50*, 395–404. https://doi.org/10.1590/0100-3984.2015.0209.
6. Quaia, E. *Contrast Media in Ultrasonography: Basic Principles and Clinical Applications*; Springer: Berlin/Heidelberg, Germany, 2005.
7. Cosgrove, D. Ultrasound contrast agents: An overview. *Eur. J. Radiol.* **2006**, *60*, 324–330. https://doi.org/10.1016/j.ejrad.2006.06.022.
8. Frinking, P.; Segers, T.; Luan, Y.; Tranquart, F. Three Decades of Ultrasound Contrast Agents: A Review of the Past, Present and Future Improvements. *Ultrasound Med. Biol.* **2020**, *46*, 892–908. https://doi.org/10.1016/j.ultrasmedbio.2019.12.008.
9. Jong, N.; Emmer, M.; Wamel, A.; Versluis, M. Ultrasonic characterization of ultrasound contrast agents. *Med. Biol. Eng. Comput.* **2009**, *47*, 861–873. https://doi.org/10.1007/s11517-009-0497-1.
10. Strouthos, C.; Lampaskis, M.; Sboros, V.; McNeilly, A.; Averkiou, M. Indicator Dilution Models for the Quantification of Microvascular Blood Flow with Bolus Administration of Ultrasound Contrast Agents. *IEEE Trans. Ultrason. Ferroelectr. Freq. Control* **2010**, *57*, 1296–1310. https://doi.org/10.1109/TUFFC.2010.1550.
11. Champagnat, S.; Coiffier, B.; Jourdain, L.; Benatsou, B.; Leguerney, I.; Lassou, N. Toward a Standardization of Ultrasound Scanners for Dynamic Contrast-Enhanced Ultrasonography: Methodology and Phantoms. *Ultrasound Med. Biol.* **2017**, *43*, 2670–2677. https://doi.org/10.1016/j.ultrasmedbio.2017.06.032.
12. Dietrich, C.; Averkiou, M.; Nielsen, M.B.; Baret, R.G.; Burns, P.N.; Calliada, F.; Cantisani, V.; Choi, B.; Chammas, M.C.; Clevert, D.-A.; et al. How to perform Contrast-Enhanced Ultrasound (CEUS). *Ultrasound Int. Open* **2017**, *3*, 2–16. https://doi.org/10.1055/s-0043-123931.
13. Senneville, B.; Novell, A.; Arthuis, C.; Mendes, V.; Dujardin, P.; Patat, F.; Bouakaz, A.; Escoffre, J.; Perrotin, F. Development of a Fluid Dynamic Model for Quantitative Contrast-Enhanced Ultrasound Imaging. *IEEE Trans. Med. Imaging* **2018**, *37*, 372–383. https://doi.org/10.1109/TMI.2017.2743099.
14. Turco, S.; Frinking, P.; Wildeboer, R.; Arditi, M.; Wijkstra, H.; Lindner, J.; Mischi, M. Contrast-Enhanced Ultrasound Quantification: From Kinetic Modeling to Machine Learning. *Ultrasound Med. Biol.* **2020**, *46*, 518–543. https://doi.org/10.1016/j.ultrasmedbio.2019.11.008.
15. Hoferer, I.; Jourdain, L.; Girot, C.; Benatsou, B.; Leguerney, L.; Cournede, P.H.; Marouf, A.; Hoarau, Y.; Lassau, N.; Champagnat, S. New calibration setup for quantitative DCE-US imaging protocol: Towards standardization. *Med. Phys.* **2023**, *50*, 5541–5552. https://doi.org/10.1002/mp.16362.
16. Marouf, A.; Rahma, A.G.; Hoferer, I.; Girot, C.; Champagnat, S.P.; Hoarau, Y. Numerical Simulations for Calibration Setup for Dynamic Contrast-Enhanced Ultrasonography Imaging Protocol. *Int. J. Numer. Methods Biomed. Eng.* **2024**, *40*, e3885. https://doi.org/10.1002/cnm.3885.
17. Chen, Q.; Li, J.; Song, Y.; Chen, B.; Christopher, D.; Li, X. Pressure-Driven Microfluidic Droplet Formation in Newtonian and Shear-Thinning Fluids in Glass Flow-Focusing Microchannels. *Int. J. Multiph. Flow* **2021**, *140*, 103648. https://doi.org/10.1016/j.ijmultiphaseflow.2021.103648.
18. Recktenwald, S.; Wagner, C.; John, T. Optimizing Pressure-Driven Pulsatile Flows in Microfluidic Devices. *Lab A Chip* **2021**, *13*, 2605–2613. https://doi.org/10.1039/d0lc01297a.

19. Bejan, A.; Zane, J.P. *Design in Nature*; Doubleday: New York, NY, USA, 2012.
20. Bejan, A.; Lorente, S. *Design with Constructal Theory*; John Wiley & Sons: Hoboken, NJ, USA, 2008.
21. Miguel, A.F. Field-Theoretic Derivation of the Constructal Law from Non-Equilibrium Thermodynamics. *Symmetry* **2026**, *18*, 732. https://doi.org/10.3390/sym18050732.
22. Lee, C.; Wang, W.; Liu, C.; Fu, L. Passive mixers in microfluidic systems: A review. *Chem. Eng. J.* **2016**, *288*, 146–160. https://doi.org/10.1016/j.cej.2015.10.122.
23. Toh, A.; Wang, Z.; Yang, C.; Nguyen, N. Engineering microfluidic concentration gradient generators for biological applications. *Microfluid Nanofluid* **2014**, *16*, 1–18. https://doi.org/10.1007/s10404-013-1236-3.
24. Miguel, A.F. Toward an optimal design principle in symmetric and asymmetric tree flow networks. *J. Theor. Biol.* **2016**, *389*, 101–109. https://doi.org/10.1016/j.jtbi.2015.10.027.
25. Li, F.; Wu, F.; Wu, S.; Tang, X.; Ma, Z.; Zhou, Y. Numerical Study of Symmetric and Asymmetric T-Junctions Droplet Formation. *Langmuir* **2025**, *41*, 32358–32371. https://doi.org/10.1021/acs.langmuir.5c03917.
26. Patankar, S.V. *Numerical Heat Transfer and Fluid Flow*; McGraw-Hill: New York, NY, USA, 1980.
27. LUMASON. *(Sulfur Hexafluoride Lipid-Type A Microspheres) for Injectable Suspension, for Intravenous Use or Intravesical Use Full Prescribing Information*; Bracco Diagnostics Inc.: Princeton, NJ, USA, 2024.
28. Serrenho, A.; Miguel, A.F. Simulation and characterization of high-porosity media for aerosol particle processing: A numerical study. *J. Porous Media* **2009**, *12*, 1129-1137. https://doi.org/10.1615/JPorMedia.v12.i12.10.
29. Pepe, V.; Miguel, A.F.; Zinani, F.; Rocha, L. New insights into creeping fluid flow through dendritic networks: A constructal view. *Int. Commun. Heat Mass Transf.* **2022**, *139*, 106409. https://doi.org/10.1016/j.icheatmasstransfer.2022.106409.
30. Roache, P.J. Quantification of uncertainty in computational fluid dynamics. *Annu. Rev. Fluid Mech.* **1997**, *29*, 123–160. https://doi.org/10.1146/annurev.fluid.29.1.123.
31. Celik, I.B.; Ghia, U.; Roache, P.J.; Freitas, C.J.; Coleman, H.; Raad, P.E. Procedure for estimation and reporting of uncertainty due to discretization in CFD applications. *J. Fluids Eng.* **2008**, *130*, 078001. https://doi.org/10.1115/1.2960953.
32. Pradhan, K.; Guha, A.; Halder, P. Characteristics of pressure drop, mass flow distribution and flow asymmetry in three-dimensional branching networks based on model human bronchial tree. *Z. Angew. Math. Mech.* **2020**, *100*, e201900022. https://doi.org/10.1002/zamm.201900022.
33. Pepe, V.; Miguel, A.F.; Zinani, F.; Rocha, L. Numerical Study of Carreau Fluid Flow in Symmetrically Branched Tubes. *Symmetry* **2025**, *17*, 48. https://doi.org/10.3390/sym17010048.